NTNU – Trondheim
Norwegian University of
Science and Technology

Position Sensor for Dampers in FSAE Racing Cars

Evelyn Livermore

Master of Science in Electronics
Submission date: June 2012
Supervisor: Hefeng Dong, IET
Co-supervisor: Petter F. Schmedling, Techni AS

Norwegian University of Science and Technology
Department of Electronics and Telecommunications

Problem Description

Techni AS has developed an ultrasonic position sensor for use on hydraulic cylinders. There is a desire to produce a functioning prototype of this position sensor for dampers for application on the racing car built by Revolve NTNU. This application requires an accuracy of sub-mm while still having a bandwidth where the dynamic response is high enough to be used in an adaptive control system for Revolve NTNUs need.

The physics behind the sensor method will be investigated and partly modeled in COMSOL Multiphysics. Results during calculations will determine if its possible and worthwhile to create a prototype. Consideration to Revolve NTNUs requirements and existing system will be discussed.

Abstract

Background Electromagnetic Acoustic Transducers are increasingly applied for Non-Destructive Testing purposes in harsh environments because of their high resistance to temperature changes and shocks when compared with traditional piezoelectric transducers which require couplants. Their most significant drawback is their low Signal-to-Noise Ratio, which increases the difficulty of design of matching networks, signal coils and choice of magnet size and type. A study of the use of an EMAT configuration developed by Techni AS applied to Formula SAE dampers is reported here.

Results and conclusion The dispersion characteristic for Rayleigh surface waves and previous articles on the propagation of horizontal polarized shear waves show that Rayleigh waves are most interesting for this application. There is no dispersion associated with Rayleigh surface waves, but additional vertically polarized waves may be excited with the Electromagnetic Acoustic Transducer (EMAT) configuration. A simple method of crosscorrelation to identify the signal from the noise has been outlined and may be implemented using an Field-Programmable Gate Array. The existing damper sensors use high-resistivity thin-films to monitor the movement of dampers. EMATs offer a lower cost alternative which may match the resolution required. However, mounting on small dampers is quite difficult, and changes in the racing car design during the thesis made it difficult to find a working solution. A positioning where the sensor works as both the bumpstop and a sensor is presented, and suggestions for improving the Signal-to-Noise Ratio (SNR) with ferrite or Soft Magnetic Flux Concentrators back-planes are introduced.

Sammendrag

Å konkurrere med racerbiler i den moderne verden krever en god forståelse av bilens kjøreegenskaper. Dette oppnås idag både ved å kjøre mye, og ved å analysere data før og etter en trening/konkurranse. Dataen samles inn enten ved alenestående dataloggere eller ved hjelp av motorstyringsenheten. Hastighet på hjul, g-krefter, temperaturer, trykk, bevegelse på dempere og ratt hentes fra sensorer montert ved forskjellige deler på bilen. De tre viktigste kravene til disse sensorene er: høy nøyaktighet, hardfør og ikke hindre bilens kjøreegenskaper.

Elektromagnetiske akustiske transdusere blir idag brukt i store industrielle miljø, som ved rørinspeksjon eller togskinneinspeksjon. De gir muligheten for ikke-destruktiv testing på ledende materialer. Deres fordeler fremfor piezoelektriske transdusere er mangelen på kontakt og muligheten for hardere miljø med større temperatur og trykkendringer. I denne oppgaven ble muligheten for å bruke elektromagnetiske transdusere som bevegelsessensorer på støtdempere i FSAE racerbiler undersøkt.

To forskjellige bølgetyper ble vurdert, Rayleigh og skjær-horisontal bølge. Horisontal polarisert skjærbølge har ikke konversjon til andre bølgetyper ved refleksjon, men har høy demping ut fra transduseren i longitudinal retning. Rayleighbølgen er dispersjonsfri, men konfigurasjonen av transduseren vil også eksitere longitudinelle bølger og det er vanskelig å skille modene fra hverandre. Konfigurasjon av mottaker- og sendespolen ble diskutert. Chirpspole var fordelaktig for å bedre signal-støy-forhold uten å miste den temporale oppløsningen, og forsterkerspole ga flere muligheter for konfigurasjon av puls. Et forslag om å bruke krysskorrelasjon som enkel støyfjerningsalgoritme ble presentert.

Denne oppgaven tar for seg utvekslingen av elektromagnetisk energi til akustiske bølger. Muligheten for multifysiske simuleringer er da viktig. Elementmetoden muliggjør simulering av multifysiske problemer. Simulering av problemet i elementmetoden ble utført i COMSOL Multiphysics. Resultatene samsvarte med analytisk teori presentert underveis. Man kom frem til at avstanden mellom spolen og det ledende materialet hadde mest å si for effektiviteten til transduseren grunnet endringen av den dynamiske magnetiske feltstyrken.

Videre transiente simuleringer viste en god overføring av elektromagnetisk energi til mekanisk energi i nærheten av magneten. Det var sammenheng mellom de mekaniske bevegelsene og pulsen sendt inn, men de mekaniske bevegelsene ble raskt dempet. Dette kan komme av numerisk demping, hvor enten den temporale

eller spatielle oppløsningen ikke var høy nok. Økning av spatiell oppløsning ga en ikke-konvergent løsning. Det oppstod asymptoter ved nanosekund-oppløsning, og disse ble forsøkt fjernet ved å øke den temporale oppløsningen. Denne økningen gjorde at simuleringen ikke fullførte, grunnet manglende diskplass. Videre feilsøking på den numeriske dempingen og asymptotiske oppførselen var utenfor denne oppgavens rammer, men bør undersøkes hvis det skal arbeides mer på.

Virkemåten til en elektromagnetisk transduser ble beskrevet, og forskjellige plasseringer av denne på en demper ble vurdert. Man kom frem til at den beste plasseringen var ved bunnen av demperen, ved støtputen. Der var det mulig å ikke ødelegge for demperens bevegelse og det var enkelt å føre ut en kabel for å koble signalet til sensoren.

På grunn av den korte tiden var det ikke mulig å lage en fungerende modell for bruk på Formula Society of Automotive Engineers (Formula SAE)-dempere. Videre testing og undersøkelse bør gjøres for å finne ut om transduseren kan sende ut signaler dekket av en støtpute. I tillegg må en verifisere at feltet blir stort nok med en så liten magnet. En burde også undersøke hvilken effekt det gir for å bedre signal-til-støy forholdet ved hjelp av Soft Magnetic Flux Concentrators (MFC) eller ferrittplate mellom spole og magnet.

Foreword

The thesis was written during spring 2012 with the supervision of Professor Hefeng Dong, Department of Electronics and Telecommunications, Norwegian University of Science and Technology. Techni AS provided the task together with the student organization Revolve NTNU.

I would like to thank my supervisor Hefeng for all the guidance during the theoretical work with the thesis. Also the people at Revolve NTNU for their patience with answering questions related to product development and the racing car. Finally, I would like to thank my friends, especially my fellow master students at the study room Fragleberg, and family for listening to me talk about the thesis topic all spring and providing good feedback.

Contents

List of Figures

Abbreviations and Acronyms

FPGA Field-Programmable Gate Array

G-force Gravity Force

EMAT Electromagnetic Acoustic Transducer

AC Alternating Current

NDT Non-Destructive Testing

SH Shear Horizontal

SV Shear Vertical

L Longitudinal

P-SV P-polarized - Shear Vertical

PPM Periodic Permanent Magnet

PML Perfectly Matched Layer

FEM Finite Element Method

Revolve Revolve NTNU

NTNU Norwegian University of Science and Technology

Formula SAE Formula Society of Automotive Engineers

EMC Electromagnetic Compatibility

SNR Signal-to-Noise Ratio

DAS Data Acquisition System

PCB Printed Circuit Board

FWHM Full Width at Half Maximum

MFC Soft Magnetic Flux Concentrators

Nomenclature

$\vec{J}$	Current Density
$\vec{E}$	Electric Field Intensity
$\vec{D}$	Electric Flux Density
$\vec{H_{ME}}$	Magnetic Field Intensity
$\vec{B}$	Magnetic Flux Density
ρ	Material Density
ε	Permittivity
μ_p	Magnetic Permeability
$\vec{F_L}$	Lorentz Force
δ	Skin Depth
f	Frequency
σ	Conductivity
Λ	Wavelength
λ	Lamé's First Parameter
μ	Shear Modulus
ω	Angular Frequency
χ	Wave Number
$\beta = \sqrt{\frac{\mu}{\rho}}$	Shear Wave Velocity
$\alpha = \sqrt{\frac{\lambda+2\mu}{\rho}}$	Pressure Wave Velocity
ν	Poisson's Ratio

Chapter 1

Introduction

This chapter gives an introduction to the report. Section 1.2 describes the motivation for the work that has been done, and a description of the student organization Revolve NTNU (Revolve). Following this, a section describing the approach to the work is given. Lastly, Section 1.4 describes the structure of the thesis.

1.1 Description

The thesis will investigate how an existing sensor system using EMAT technology may be applied to the dampers of the racing car for Revolve. The lean product development theory has been followed in the racing car design process, and some consideration to this has been taken for the thesis as well.

The thesis topic was chosen because of the author's involvement in the student organization Revolve.

1.2 Motivation

The motivation for monitoring the position of dampers in a racing car is to be able to adjust their stiffness and normal position during the race. In order to win a race, one wants to regulate the dampers so that the tires have maximum contact with the tarmac at all times. There are two obstacles to achieving this — an uneven road and unbalanced turns, the latter of which is quite common. If the suspension is set equally for all four dampers, the inner wheels will lift off during a turn. This can be compensated for by stiffening the outer wheels' suspension and softening the inner wheels'.

A racing track and any car environment are considered harsh environments, so the position sensor equipment must be able to perform under such conditions. G-forces experienced during turns and accelerations, as well as large variations in temperature are significant issues. Non-destructive measurement to avoid damaging the suspension qualities of the dampers is necessary. The goal is to find a

sensor system which will enable real-time monitoring of the dampers' movement, while neither damaging the suspension nor interfering with the driving experience.

The key factor for the sensor system to be successful, is that the customer Revolve be satisfied with its performance. The requirements necessary for success are described in section 2.2.

Revolve NTNU

Revolve NTNU is a student organization at the Norwegian University of Science and Technology (NTNU). It was founded in the late fall of 2010 with the goal of designing, building and competing with a Formula Student car for the 2012 season. Formula Student is an international competition which takes place at the Silverstone Formula 1 arena in the UK each year. Designing and building a racing car from scratch, that will be tested in both static and dynamic events, is the challenge in which several hundred teams try to best each other.

The teams are asked to simulate that they receive an order for a prototype racing car for evaluation. The customer is a non-commercial amateur driver, and the number of cars to be produced is 1000. The car must be reliable, easy to maintain and cheap — while still performing exceptionally and giving the driver the thrill of his/her life [23].

The static events include a presentation, a thorough cost analysis, and a scrutinizing process in which the team has to defend all design choices down to every detail. It is not enough to justify the choice of e.g. engine position with "it has been done before by a team last year and it gave them good results". All design decisions must show comprehensive background research and simulations.

The dynamic events test the car's performance in acceleration, handling and endurance. Here the teams get a chance to show off and prove that they have designed cars built for the hard racing environment. Fuel consumption is evaluated, adding the extra challenge which is also a part of the commercial car business - environment conscious high performance vehicles.

Revolve consists of 35 students from different engineering programmes at Norwegian University of Science and Technology. The author is the group leader of electronics and engine management. The other areas of responsibility include frame and chassis, engine and drivetrain, suspension and brakes, and vehicle control and safety. The biggest challenge in designing a car is making the trade-offs necessary so that all the parts fit together and optimize the car's performance in the dynamic events. Each student has spent approximately 20 hours a week since the beginning of 2011, and the workload has increased to about 30 hours since Easter 2012, giving a total of 40 000 work hours.

For the electronics and engine management group, the goal has been to equip the racing car with the equipment necessary to provide the driver with all the desired feedback and data needed to improve driving experience and performance. In order to achieve this goal, it is essential that all parts which are subject to stress and change be monitored individually, and reviewed and analyzed both during and after a race.

1.3 Work

First, a literature study of existing EMAT systems was done, and the physics behind their function understood. The dispersion characteristics of two wave types, Shear Horizontal (SH) and Rayleigh surface waves, were investigated. The latter has been developed by the company as the configuration of the EMAT for sensing distance was simpler. There are advantages and disadvantages with both wave modes, and these were discussed briefly in the thesis. Rayleigh waves only were simulated on the damper rod as this was the final configuration.

The validity of using COMSOL Multiphysics as Finite Element Method (FEM) software for EMAT was checked by investigating the dynamic magnetic field, static magnetic field and eddy current generation separately.

Analyzis of the EMAT mounting on dampers was performed, and attention was given to signal propagation and simpleness of design. Finally, a conclusion regarding implementation of EMAT sensor system on the dampers in use at Revolve has been outlined.

1.4 Structure of Report

Chapter 2 The background theory of EMAT technology and employment in Non-Destructive Testing (NDT) is discussed. Section 2.2 describes the current sensor system employed on the racing car. The requirements set by Revolve are also outlined.

Chapter 3 Section 3.1.1 and 3.1.2 derives and investigates the dispersion characteristics for SH and Rayleigh surface waves respectively. Section 3.2 discusses signal generation and receiving for EMATs, as well as the cross-correlation used to enhance signal identification.

Chapter 4 A description of the new damper system and discussion of various placements is given in Section 4.1. Following this, the modeling process in COMSOL Multiphysics is outlined and results from simulations are given and discussed.

Chapter 5 Final thoughts and future work are presented. New placement for EMAT for use as position sensor for Formula SAE dampers introduced, as well as ideas for improvements of Signal-to-Noise Ratio.

Figure 1.1: KA Borealis R rear. Copyright: Sofie Brovold

Chapter 2

Background

This chapter presents the electromagnetic and acoustic wave theory behind the work that has been done for the thesis. The first section will explain the principle of EMAT operation in relation to conducting surfaces, here exemplified by a cylinder. Previous work in NDT will be exemplified with different EMAT configurations. The damping system and existing sensor type is explained in Section 2.2. Section 2.3 outlines the derivation of Navier's equation.

Throughout the thesis, non-ferromagnetic materials are considered. Further, a quasi-static electromagnetic field is assumed, so that the displacement current is neglected. This leads to regarding "the mechanism of energy transfer as diffusion rather than a wave, which is analogous to heat transfer" [14]. This is valid when $\vec{J}(r,t) >> \tau_{max}\frac{\partial \vec{J}(r,t)}{\partial t}$, where τ_{max} is the time between the two points furthest from each other.

2.1 EMAT

An electromagnetic acoustic transducer uses electromagnetic energy to produce pressure waves in a conducting surface — acoustic waves. It consists of a magnet which produces a static magnetic field $\vec{B}_s$ and an electric coil which is driven at ultrasonic frequency. The driving current can either be continuous or configured as a pulse, depending on the type of ultrasonic wave is desired. The transducer is placed near a metallic conducting surface, e.g. a metal.

2.1.1 Theoretical Background

Maxwell's equations, given in Eqs. 2.1 to 2.4, together with the constitutive relationships in Eqs. 2.6 and 2.5, govern the electromagnetic field. The quantities described here are defined in Table 2.1.

$$\nabla \times \vec{E} = -\frac{\delta \vec{B}}{\delta t} \tag{2.1}$$

$$\nabla \cdot \vec{D} = \frac{\rho}{\varepsilon} \tag{2.2}$$

$$\nabla \times \vec{H_{ME}} = \mu_p \vec{J} + \mu_p \varepsilon \frac{\delta \vec{E}}{\delta t} \tag{2.3}$$

$$\nabla \cdot \vec{B} = 0 \tag{2.4}$$

where μ_p is the permeability, ε the permittivity, ρ the total charge density, and $\vec{J}$ the total current density.

$$\vec{D} = \varepsilon \vec{E} \tag{2.5}$$

$$\vec{H} = \frac{1}{\mu_p} \vec{B} \tag{2.6}$$

Table 2.1: Electromagnetic Field Quantities

Name	Symbol	Unit
Electric field intensity	$\vec{E}$	V/m
Electric flux density	$\vec{D}$	C/m^2
Magnetic field intensity	$\vec{H}$	A/m
Magnetic flux density	$\vec{B}$	T

From this it is possible to derive Lorentz force[1] equation, Eq. 2.7, which gives the external force acting on the cylinder.

$$\vec{F_L} = \vec{J_e} \times \left(\vec{B_s} + \vec{B_d} \right) \tag{2.7}$$

where $\vec{B_d}$ is the dynamic magnetic field.

When providing an Alternating Current (AC) $\vec{J_{AC}}$ to the electric coil, an eddy current, $\vec{J_e}$, will be induced on the cylinder surface. The eddy currents[2] are influenced by the magnetic field and a Lorentz force is set up [5], given by equation 2.7. The depth to which the currents actually penetrate may be characterized by the skin depth, given by $\delta = \frac{1}{\sqrt{\pi f \sigma \mu_p}}$, where σ is the conductivity and f is the frequency of the wave.

A plot of skin depth as a function of frequency is given in Figure 2.1 for stainless steel of parameters given in Section 4.2.2.

[1] Lorentz force: the force a moving point charge experiences due to an electromagnetic field.

[2] Eddy currents are small electric currents which arise from circulating flow of electrons driven by a changing magnetic field. The eddy currents are mainly contained in the skin layer of the material.

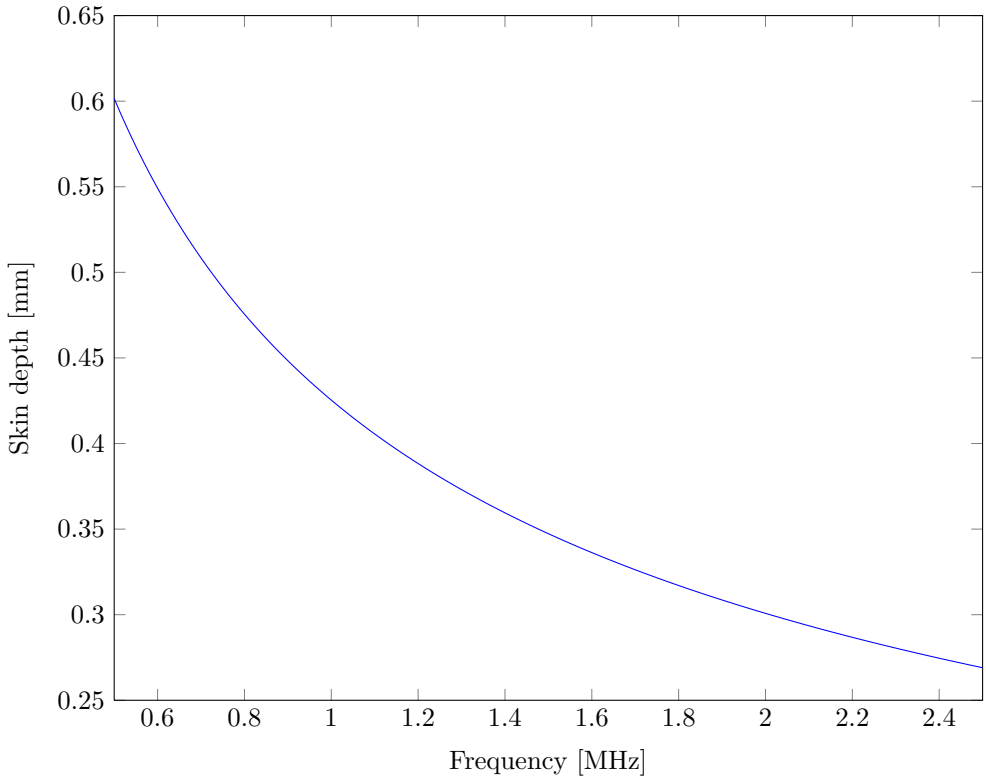

Figure 2.1: Depth of penetration for eddy currents.

It is important that the static magnetic field penetrate deeply and strongly enough at the given skin depth, so that it interacts with the eddy currents to cause acoustic waves. The dynamic magnetic field, the static magnetic field and the eddy currents will be investigated in Chapter 4.

The standard configurations of EMAT employ the static magnetic field as the dominating field. This is because creating a strong dynamic field requires a high driving current which would make the system more hazardous. However, a strong static magnetic field requires the use of either rare-earth permanent magnets or electromagnets. The prior will need to be of a certain size to create the necessary field, and the latter requires extra electronics. Most applications use rare-earth permanent magnets and sacrifice size for simplicity and durability. A problem with rare earth magnets is that they are conductive [15, p.72]. This may cause an EMAT magnetostriction effect, resulting in high-frequency acoustic waves inside the magnets. These acoustic waves will in turn interfere with the signals from the conductive material.

The interaction between the two magnetic fields creates an ultrasonic wave which propagates through the material. The type of ultrasonic wave generated depends on the configuration of the EMAT and the driving electric current.

EMATs offer one big advantage over traditional piezoelectric transducers as they do not require a couplant to the surface, only proximity. A couplant typically reduces the signal power, and requires careful mounting of the transducer. Additionally, EMATs can be used in a wider temperature range; below the freezing point of couplants and above their boiling point. However, the seperation between the conducting surface and the EMAT cannot be too great, because of signal loss through air.

The greatest disadvantage of EMATs is the low SNR. Furthermore, they are very sensitive to what material the conductive surface is. An EMAT system which works well for one type of steel, may not work with a different type — even though the physical size and shape are equal. Moreover, the use of EMAT requires a conducting or ferromagnetic material. It is not possible to use the EMAT technique to inspect other typical materials such as composites and plastics.

2.1.2 EMAT Configuration and NDT

Depending on the configuration of the EMAT, different types of waves are excited. Typically, if the magnetic field is perpendicular to the surface, a shear wave displacement will be excited. The other case, when the magnetic field is parallel to the surface, will excite longitudinal waves. Figure 2.2 gives various configurations to excite the different modes on flat surfaces. Depending on the application, these may be modified to fit the desired geometry while exciting the modes required for the specific application.

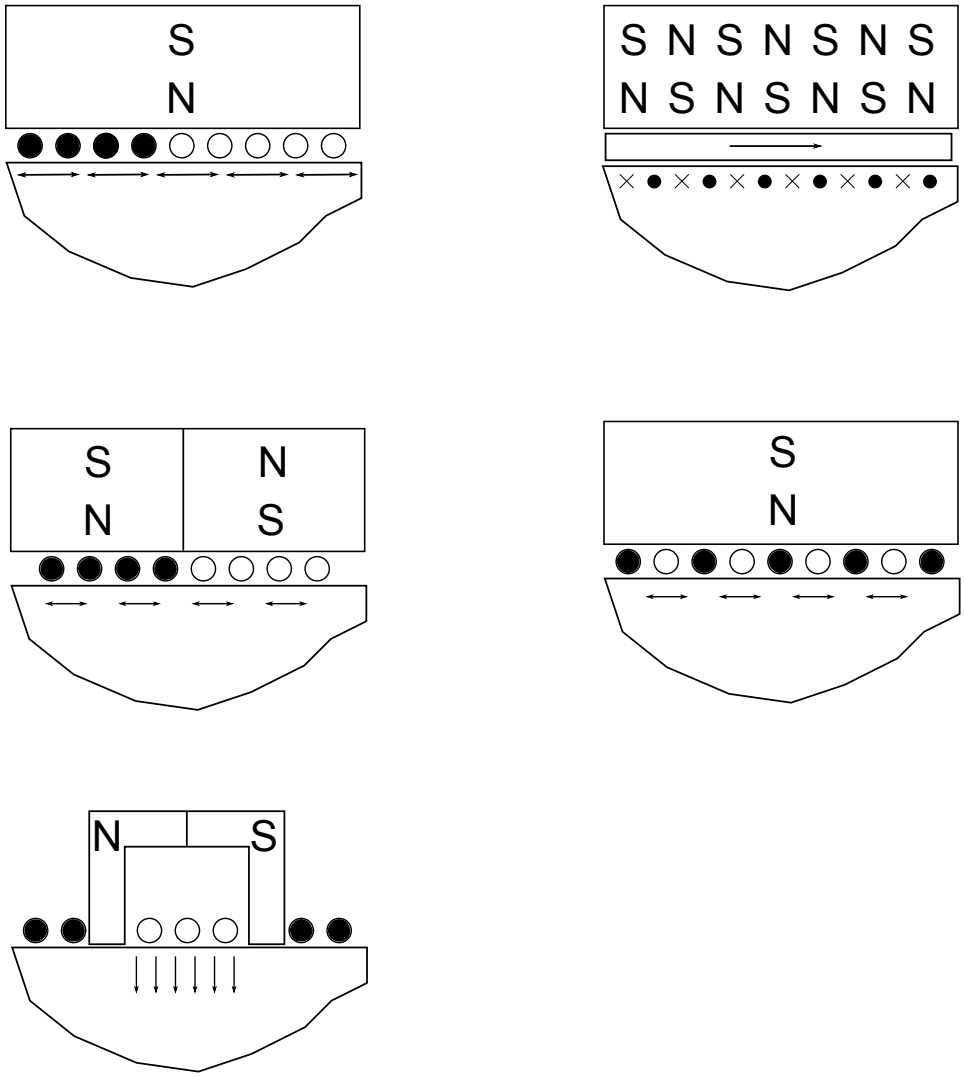

Figure 2.2: Various EMAT configurations. Top left: Spiral coil EMAT for excitation of radially polarized shear waves. Top right: Periodic permanent magnet EMAT for surface SH generation. Middle left: Normal field EMAT for excitation of shear waves propagating normal to the surface. Middle right: Meander coil EMAT for surface L or SV waves in plates. Bottom left: Tangential field EMAT for excitation of longitudinal waves propagating normal to the surface. The 'N' and 'S' indicate the polarity of the magnets for these and subsequent figures. Figures adapted from [5] and [25].

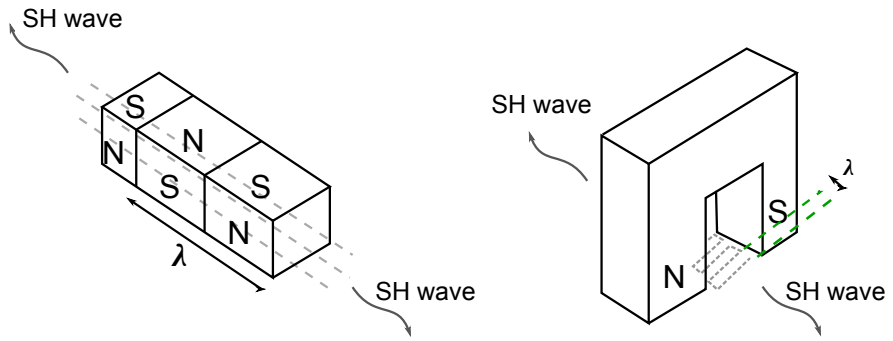

Figure 2.3: SH wave excitation in plates. Light gray dashed lines represent the AC coil. Left: PPM configuration. Right: Magnetostrictive EMAT. Adapted from [25]

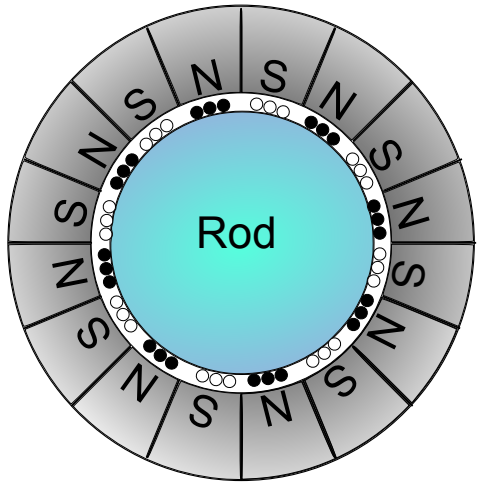

Figure 2.4: Cross-section of EMAT for rod inspection creating torsional modes. The small circles represent wires, the filling indicating opposite current flow. Figure adapted from [18].

EMATs have been used successfully in several non-destructive testing environments such as velocity dependence on temperature [20] and welding inspection. EMATs have also been used in greater industrial applications such as railway in-

spection [16], or buried pipelines [1].

In [27], Yibo successfully detects artificial flaws on a hollow cylinder, see Figure 2.5, using both the lowest longitudinal and torsional mode. This paper also highlights the varying types of reflection caused by circular geometric flaws and non-symmetric corrosion. Even though the longitudinal mode is able to detect all the artifical flaws, it is greatly attenuated after passing three flaws and should not be used for multiple flaw detection. The torsional mode has a higher signal amplitude at the flaws, but is more sensitive to the length of the pipe than the longitudinal mode. The choice of mode depends heavily on the application and is an important part of the development process.

A significant advantage of using SH polarized waves compared to vertical polarized shear waves such as P-polarized - Shear Vertical (P-SV), is that there is no coupling between P and SH, no mode conversion or phase shift at reflections [11]. This simplifies the design of the EMAT, and the signal processing necessary to get accurate results. SH modes in plates are often excited using a Periodic Permanent Magnet (PPM) configuration as shown top left in Figure 2.3. The frequency of a PPM-EMAT depends on the spacing of the magnets, and this causes a natural drawback for high frequency operation. The magnets lose their efficiency when the magnets are very thin, making it difficult to get a high enough SNR for short wavelengths.

The corresponding configuration for rods is given in Figure 2.4, as the torsional mode of a rod is equivalent to, and governed by the same set of equations, as SH waves in plates. Johnson et. al used the configuration given in Figure 2.4 to measure the distance with a trapped torsional mode in a rod. However, they found that this configuration had a steep amplitude drop-off. The amplitude decreased by two orders of magnitude when the distance increased threefold.

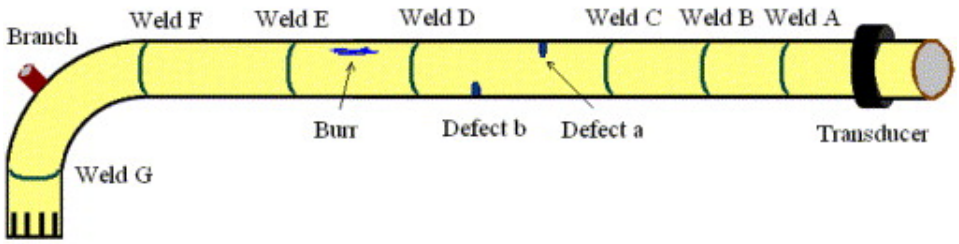

Figure 2.5: Drawing from [27] of pipe characteristics and defects.

A Rayleigh surface wave may be excited using the configuration shown middle right in Figure 2.2. The drawback of using this configuration is that not only Rayleigh surface waves are excited, but also longitudinal waves in the bulk of the conducting medium. Thus it is more difficult to separate the modes, and the receiver must be configured to pick up only the Rayleigh surface wave signal. The velocity of the longitudinal modes are generally twice that of the Rayleigh modes — which eases the process of discerning the modes.

2.2 Damper System

The damper system of the racing car designed by Revolve uses special Formula SAE twin tube dampers. These are outfitted with springs to return them to normal position after compression/expansion. Revolve has several spring sets available, with stiffness ranging from 150 lb/in to 650 lb/in.

Figure 2.6: Ohlins twin tube Formula SAE damper. See appendix C for a detailed interior figure.

Choosing the correct spring set is a process in which several aspects must be considered. First the ride frequency must be determined (low for passenger cars (0.5 – 1.0 Hz), higher for racing cars (3.0 Hz – 5.0 Hz or more)). High frequencies lower the center of gravity but create less suspension. Additionally, these frequencies should be different for the front and rear suspension as the front and rear of the car pass bumps and uneven spots at different times.

Finally, after selecting the ride frequency, the spring rate is determined from this frequency, sprung mass of each wheel, and the motion ratio of suspension [12]. After choosing the spring rate test runs should be made with different drivers to determine if the chosen suspension is what they want. After all, the driver's comfort and the racing car's driveability is what is most important.

The springs are fastened by suspending them between top and bottom circular faces, shown in Appendix C. The bottom face is removable, with an opening equal to the diameter of the rod.

Existing Damper Sensors

The existing damper sensors are high-quality linear position sensors. They use a high resistivity conductive plastic film which is both mechanically and electrically bonded to a wirewound potentiometer. This type of sensor was chosen for monitoring the dampers' movements for the following reasons [6].

Low cost It is based on simple electronics and uses low current. The low cost is important to Revolve as all funds must be supplied from sponsors, nothing is provided by the students themselves or the university.

Good Electromagnetic Compatibility (EMC) A racing car is a very noisy environment for signals. Especially the solenoid for gearshifting, and the ignitors for the engine cause large amounts of pulsed noise during driving. It is important that the sensors are resistant to electromagnetic noise so that the signals do not get corrupted. Corrupted signals may lead to false positives and negatives, which in turn causes the analysis of driving to be faulty and unrealiable.

Easy and simple installation This sensor type features multiple mounting accessories, and the customer does not need special or expensive tooling to mount. As the goal of the competition is to create a prototype racing car for non-professionals, this is an important factor in choosing sensors — they must be simple to maintain and change if necessary.

Linearity When setting up the system for the first time, linearity is a positive feature for tuning the data acquistion. It simplifies setup and does not require time-consuming calculations.

High resolution The manufacturer claims to have infinite resolution. This is probably not true, but may be interpreted as having good enough resolution for what is necessary for small damper movements. By having a high resolution, the data acquisition is not limited by the sensor, but rather by the amount of data sampled and required by the user.

These characteristics are requirements which a new sensor must meet in order to be considered as a replacement by Revolve. The product development process follows the model given in figure 2.7 from Roozenburg and Eekels [26], where the "evaluation" phase is the defining phase for Revolve.

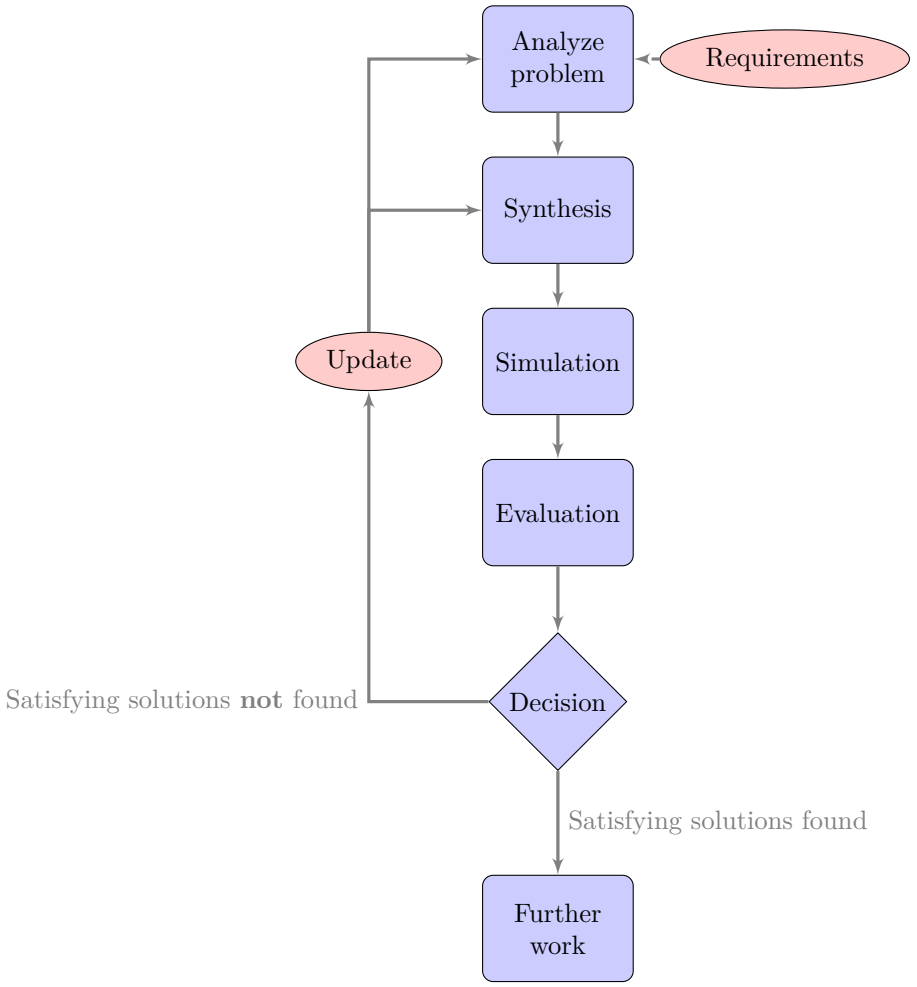

Figure 2.7: Phases in a product development process

2.3 Ultrasonic Wave

For the thesis, all materials are assumed to be homogeneous, isotropic elastic materials. Elastic materials return to their original shape after experiencing a force, i.e. no deformation occurs. The ultrasonic wave used in this project will not stress the materials beyond this. The motion of the medium may be described by the following equation [9].

$$\mu\nabla^2\vec{u} + (\lambda + \mu)\nabla\nabla \cdot \vec{u} = \rho\left(\frac{\partial^2\vec{u}}{\partial t}\right) \tag{2.8}$$

where $\vec{u}$ represents the displacement vector, ρ is the density, λ and μ are Lamé

constants. This equation is derived from Newton's 2nd law

$$\vec{F} = m\vec{a} = m\frac{\partial^2 \vec{u}}{\partial t^2} \tag{2.9}$$

where $\vec{u}$ is the displacement vector. By employing Newton's 2nd law to the stress σ_{ij} a body experiences when an external force is applied, it can be rewritten as

$$\sigma_{ij,j} + f = \rho\frac{\partial^2 \vec{u}}{\partial t^2} \tag{2.10}$$

where $,j$ represents differentiation with respect to the i^{th} coordinate and f external force. In order to arrive at Navier's equation, Hooke's law describing the linear relationship between strain and stress is employed.

$$\sigma_{ij} = c_{ijkl}\epsilon_{kl}, \tag{2.11}$$

$$\epsilon_{kl} = \frac{1}{2}(u_{k,l} + u_{l,k}) \tag{2.12}$$

where c is a 4th order elasticity tensor, and ϵ_{kl} the strain tensor described by Eq. 2.12. Due to symmetry, only 21 of the 81 coeffiecients are independent, and for isotropic, homogeneous elastic materials, there are only 2 independent coefficients. These are the 1^{st} and 2^{nd} Lamé constants, λ and μ, which we recognize from Eq. 2.8. This simplifies Eq. 2.11 to

$$\sigma_{ij} = \lambda\epsilon_{kk}\delta_{ij} + 2\mu\epsilon_{ij} \tag{2.13}$$

where δ_{ij} represents the Kronecker delta function[3].

Finally, by combining Equations 2.10 and 2.13 we arrive at Navier's equation. Navier's equation has an infinite number of solutions. Defining boundary conditions and source conditions are necessary to solve for a given situation and determine a solution.

Wave Types

There are three main types of waves which may exist in an elastic solid. These are

Torsional waves
: These are characterized by a twisting of the medium, such as a wire or a rod.

Flexural waves
: Flexural waves are also called transverse waves. The particle displacement is transversal to the direction of wave propagation. Flexural waves may also be called shear waves.

[3] Kronecker delta function $\delta_{ij} = \left\{ \begin{array}{ll} 1 & \text{if } i = j \\ 0 & \text{if } i \neq j \end{array} \right\}$

Longitudinal waves

When the particle displacement is parallel to the direction of wave propagation, the waves are called longitudinal or compression waves.

Combination of these wave types is also possible. In order to determine which modes are present at various frequencies and depths, the dispersion relation will be derived in the following section. The dispersion relation describes how the wave propagation is affected by frequency, and is related to the material characteristics as well as the wave type. Two cases are considered, SH and Rayleigh surface waves, because of their aforementioned advantages.

Chapter 3

Signal Propagation

In Section 3.1 the dispersion relation of both SH-waves and Rayleigh surface waves is derived, and their characteristics are plotted for the lowest modes of SH-waves and the Rayleigh surface wave mode. A description of the transmitting and receiving of signal is given in Section 3.2. Following this, a description of the existing model developed in-house at Techni AS is given, along with a discussion of the measurements performed is outlined.

3.1 Dispersion Relation

A cylindrical coordinate system is chosen, and given in Figure 3.1. This is valid for both dispersion relations due to the cylindrical symmetry of the piston rod.

3.1.1 Horizontal Polarized Shear Waves

Because of the cylinder and the small wavelength, plane waves are assumed and that they are independent of θ. Further, the displacement is assumed to be solely in the r-direction, not z-direction (consistent with SH-waves). This causes the solution of particle displacement to Navier's equation to consist of the following components

$$\vec{u} = \nabla\varphi + \nabla \times \vec{H} \tag{3.1}$$

$$u_\theta = \vec{e}_\theta \Big(\frac{\partial H_r}{\partial z} - \frac{\partial H_z}{\partial r} \Big) \tag{3.2}$$

$$u_z = 0 \tag{3.3}$$

$$u_r = 0 \tag{3.4}$$

since

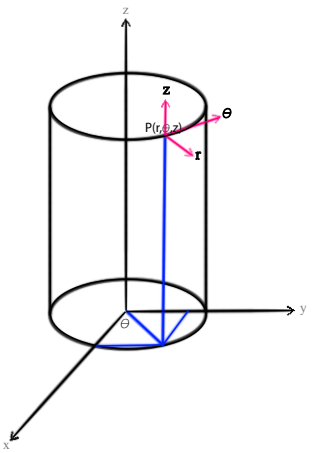

Figure 3.1: Cylindrical coordinate system

$$\begin{aligned}\nabla \times \vec{H} = \vec{e}_r\Big(\frac{1}{r}\frac{\partial H_z}{\partial \theta} - \frac{\partial H_\theta}{\partial z}\Big) \\ + \vec{e}_\theta\Big(\frac{\partial H_r}{\partial z} - \frac{\partial H_z}{\partial r}\Big) \\ + \vec{e}_z\frac{1}{r}\Big(\frac{\partial (rH_\theta)}{\partial r} - \frac{\partial H_r}{\partial \theta}\Big) \qquad (3.5)\end{aligned}$$

$$\nabla\varphi = \vec{e}_r\frac{\partial \varphi}{\partial r} + \vec{e}_\theta\frac{1}{r}\frac{\partial \varphi}{\partial \theta} + \vec{e}_z\frac{\partial \varphi}{\partial z} \qquad (3.6)$$

φ is the dilatational (compression wave) scalar potential and $\vec{H}$ is an equivoluminal vector potential. The constants α and β are, respectively, the pressure and shear wave velocities. However, with the shear horizontal wave there is no dilatational component present, and solving the particle displacement for φ may be disregarded. Further, shear horizontal waves assume only u_θ displacement field [13, p.468], which is true only if $H_z \neq 0$ is assumed. $\vec{H}$ must satisfy the following wave equation

$$\beta^2\nabla^2\vec{H} = \frac{\partial^2\vec{H}}{\partial t^2} \qquad (3.7)$$

where $\beta^2 = \frac{\mu}{\rho}$. Assuming plane wave harmonic propagation in z-direction, let

$$H_z = B_s F(r)\exp(i(\xi z - \omega t)) \qquad (3.8)$$

where $F(r)$ is an arbitrary function and B_s an amplitude. Eq. 3.7 gives

$$\frac{\partial^2 F(r)}{\partial r^2} + \frac{1}{r}\frac{\partial F(r)}{\partial r} + (-\xi^2)F(r) = \frac{1}{\beta^2}(-\omega^2)F(r) \tag{3.9}$$

by choosing $\frac{\omega}{\beta} = k_\beta$ and $k_\beta^2 - \xi^2 = k^2$ we get

$$\frac{\partial^2 F(r)}{\partial r^2} + \frac{1}{r}\frac{\partial F(r)}{\partial r} + k^2 F(r) = 0 \tag{3.10}$$

The first Bessel function $J_0(kr)$ is a solution to Equation 3.10 so that

$$H_z = B_s J_0(kr) \exp\Big(i(\xi z - \omega t)\Big) \tag{3.11}$$

This is then used to find the displacement component given in Equation 3.2.

$$u_\theta = kB_s J_1(kr) \exp\Big(i(\xi z - \omega t)\Big) \tag{3.12}$$

To solve the complete problem and find the dispersion relation, boundary conditions must be applied. From Equation 2.13 applied to this situation

$$\sigma_{r\theta} = \mu\Big(\frac{\partial u_\theta}{\partial r} - \frac{u_\theta}{r}\Big) \tag{3.13}$$

which is equal to 0 at the outer radius of the rod r=a. From this condition we end up with

$$k\Big[kJ_0(ka) - \frac{2J_1(ka)}{a}\Big] = 0 \tag{3.14}$$

Polynomial Roots

The first equation gives a polynomial from $k^2 = 0$ so that

$$\begin{aligned} k &= 0 \\ \frac{\omega^2}{\beta^2} - \xi^2 &= 0 \\ v_p = \frac{\omega}{\xi} &= \beta \end{aligned} \tag{3.15}$$

which is a single solution and the first mode.

Bessel Function Roots

To solve the Bessel-part of Equation 3.14, Matlab is employed and the function is plotted in Figure 3.2.

The roots of these plots were found using the `fzero` function in Matlab, where the code is given in Appendix B.1. The roots are given in table 3.1 with their corresponding cutoff-frequencies[1].

[1] The cutoff frequency is the frequency of which the modes start to exist and propagate.

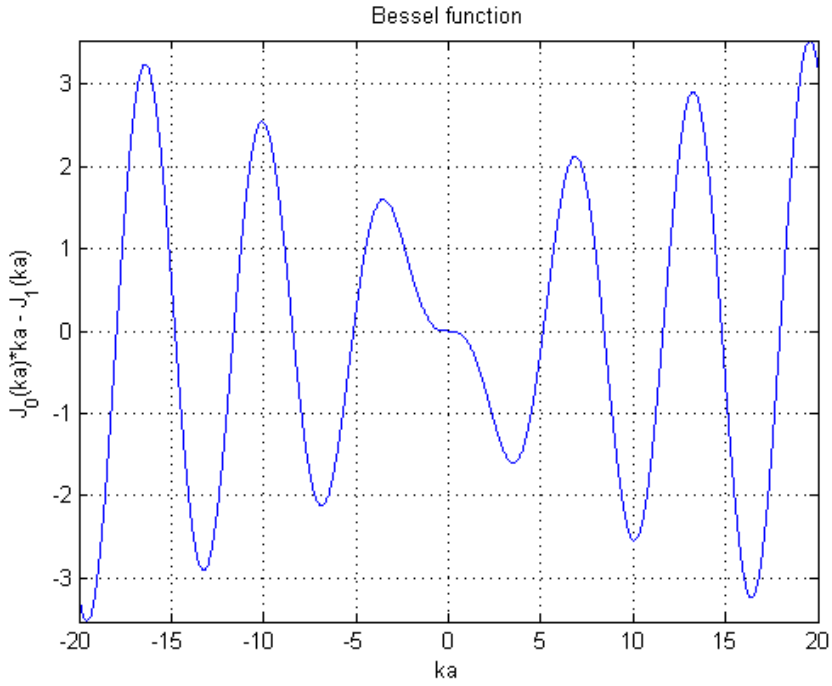

Figure 3.2: Plot from equation 3.14

Table 3.1: Table of Roots and Cut-off Frequencies

Index	Roots from equation 3.14	Corresponding cut-off frequencies [kHz]
0	0	NaN
1	5.1536	654.2
2	8.4172	1072.2
3	11.6198	1408.2
4	14.7960	1884.8
5	17.9598	2287.8

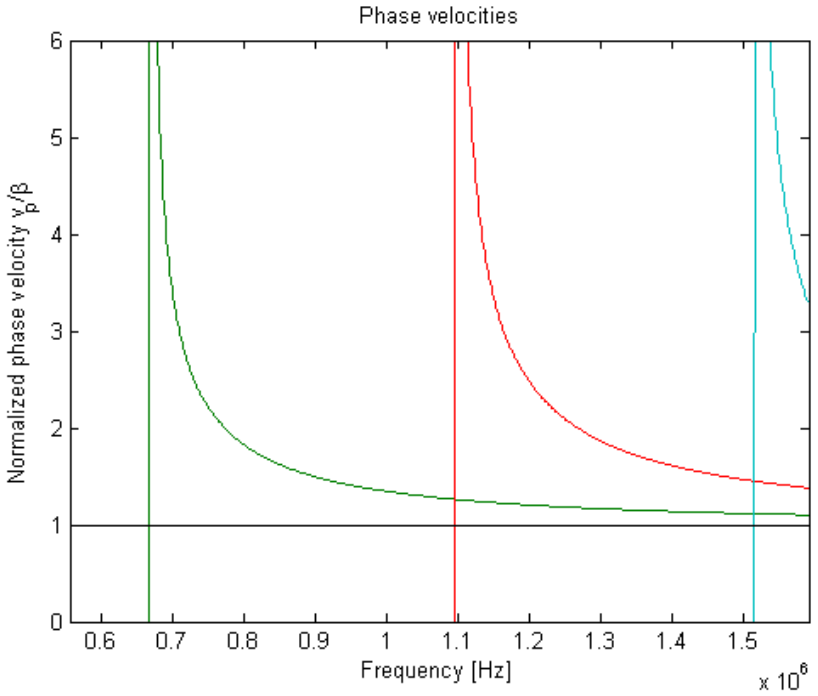

Figure 3.3: Phase velocities for the first three modes. Black: main mode $v_p = \beta$, green: first mode (ka=5.1356), red: second mode (ka=8.4172), cyan: third mode (ka=11.6198)

Finally, using the relationship $k^2 = \frac{\omega^2\rho}{\mu} - \xi^2$ yields a frequency-wave number relationship for sets of ka

$$(ka)^2 = \left(\frac{\omega a}{\beta}\right)^2 - (\xi a)^2, \text{ such that} \tag{3.16}$$

$$v_p = \frac{\omega a}{\xi a} = \frac{\omega a \beta}{\sqrt{(\omega a)^2 - (\beta k a)^2}}. \tag{3.17}$$

The phase velocities for the first three roots greater than zero are plotted in Figure 3.3.

3.1.2 Dispersion Relation - Rayleigh Surface Waves

As with SH-waves, plane waves in cylindrical coordinates are assumed. However, the propagation of the H-component is not independent of θ. In this case, the solution of particle displacement to Navier's equation to consists of both u_z and u_r.

$$\vec{u} = \nabla\varphi + \nabla \times \vec{H} \tag{3.18}$$
$$u_\theta = 0 \tag{3.19}$$
$$u_z = \frac{\partial\varphi}{\partial z} + \frac{\partial H_\theta}{\partial r} + \frac{H_\theta}{r} \tag{3.20}$$
$$u_r = \frac{\partial\varphi}{\partial r} - \frac{\partial H_\theta}{\partial z} \tag{3.21}$$

which much be solutions to the wave equations

$$\beta^2\nabla^2\vec{H} = \frac{\partial^2\vec{H}}{\partial t^2} \tag{3.22}$$
$$\alpha^2\nabla^2\varphi = \frac{\partial^2\varphi}{\partial t^2} \tag{3.23}$$

These are the same equations as for the SH-wave case. As described in [3] of Rayleigh surface wave propagation inside a borehole, H_θ consists of two components as it is tangent to the cylinder and parallel to xy-plane

$$H_{\theta x} = -H_\theta \sin(\theta), \tag{3.24}$$
$$H_{\theta y} = H_\theta \cos(\theta). \tag{3.25}$$

Solving Equations 3.22 and 3.23 for φ and $H_{\theta y}$,

$$\frac{\partial^2\varphi}{\partial r^2} + \frac{1}{r}\frac{\partial\varphi}{\partial r} + \frac{\partial^2\varphi}{\partial z^2} = \frac{1}{\alpha^2}\frac{\partial^2\varphi}{\partial t^2} \tag{3.26}$$
$$\frac{\partial^2\varphi}{\partial r^2} + \frac{1}{r}\frac{\partial\varphi}{\partial r} - \varphi\Big(0 + (\xi^2 - \frac{\omega^2}{\alpha^2})\Big) = 0$$
$$\frac{\partial^2 H_{\theta y}}{\partial r^2} + \frac{1}{r}\frac{\partial H_{\theta y}}{\partial r} + \frac{1}{r^2}\frac{\partial^2 H_{\theta y}}{\partial\theta^2} + \frac{\partial^2 H_{\theta y}}{\partial z^2} = \frac{1}{\beta^2}\frac{\partial^2 H_{\theta y}}{\partial t^2}$$
$$\frac{\partial^2 H_\theta}{\partial r^2} + \frac{1}{r}\frac{\partial H_\theta}{\partial r} - \frac{H_\theta}{r^2} + \frac{\partial^2 H_\theta}{\partial z^2} = \frac{1}{\beta^2}\frac{\partial^2 H_\theta}{\partial t^2} \tag{3.27}$$
$$\frac{\partial^2 H_\theta}{\partial r^2} + \frac{1}{r}\frac{\partial H_\theta}{\partial r} - \frac{H_\theta}{r^2}\Big(1 + (\xi^2 - \frac{\omega^2}{\beta^2})\Big) = 0,$$

where $\beta^2 = \frac{\mu}{\rho}$ and $\alpha^2 = \frac{\lambda+2\mu}{\rho}$. Functions which satisfy these are given by the zero (I_0) and first (I_1) order modified Bessel functions, respectively.

$$\varphi = \varphi_0 I_0(k_1 r)\cos(\xi z - \omega t) \tag{3.28}$$
$$H_\theta = H_0 I_1(k_2 r)\sin(\xi z - \omega t), \tag{3.29}$$

where $k_2 = \xi(1-\vartheta_1^2)^{1/2}$, $k_1 = \xi(1-\vartheta_2^2)^{1/2}$ and $\vartheta_1 = \frac{\omega}{\beta\xi}$, $\vartheta_2 = \frac{\omega}{\alpha\xi}$; by assuming harmonic propagation in z-direction.

The boundary conditions are given by Equation 2.13 and for this particular case they are

$$\sigma_{rr} = \lambda\Big(\frac{\partial u_r}{\partial r} + \frac{\partial u_z}{\partial z} + \frac{u_r}{r}\Big) + 2\mu\frac{\partial u_r}{\partial r} \tag{3.30}$$

$$\sigma_{rz} = \mu\Big(\frac{\partial u_z}{\partial r} + \frac{\partial u_r}{\partial z}\Big). \tag{3.31}$$

Using Equations 3.21, 3.20 and 3.26, 3.27 they become

$$\sigma_{rr} = \frac{\lambda}{\alpha^2}\frac{\partial^2\varphi}{\partial t^2} + 2\mu\Big(\frac{\partial^2\varphi}{\partial r^2} - \frac{\partial^2 H_\theta}{\partial r\partial z}\Big) \tag{3.32}$$

$$\sigma_{rz} = \frac{\mu}{\beta^2}\frac{\partial^2 H_\theta}{\partial t^2} + 2\mu\Big(\frac{\partial^2\varphi}{\partial r\partial z} - \frac{\partial^2 H_\theta}{\partial z^2}\Big) \tag{3.33}$$

Using Equations 3.29 and 3.28, the second boundary condition gives a ratio for $\frac{\varphi_0}{H_0}$. While the first boundary condition gives Equation 3.35. For details, please see Appendix A.

$$\frac{\varphi_0}{H_\theta} = \frac{I_1(k_2 r)(2-\vartheta_1^2)}{-2(1-\vartheta_2^2)I_1(k_1 r)} \tag{3.34}$$

$$\begin{aligned} 0 = {} & -b\vartheta_1^2\varphi_0 I_0(k_1 r) + 2\varphi_0(1-\vartheta_2^2)\Big[I_0(k_1 r) + \frac{I_1(k_1 r)}{k_1 r}\Big] \\ & + 2H_0(1-\vartheta_1^2)^{1/2}\Big[I_0(k_2 r) + \frac{I_1(k_2 r)}{k_2 r}\Big] \end{aligned} \tag{3.35}$$

where $b = \frac{\nu}{1-\nu}$. ν is Poisson's ratio.

By combining these two we arrive at a single Equation 3.36 describing the wave propagation of surface Rayleigh waves. This is valid when r=a, and the final equation is given as.

$$\begin{aligned} 0 = {} & 4(1-\vartheta_1^2)^{1/2}\Big[\frac{I_0(k_2 a)}{I_1(k_2 a)} + \frac{1}{k_2 a}\Big] \\ & - 2\frac{(2-\vartheta_1^2)(1-\vartheta_2^2)^{1/2}}{k_1 a} - \frac{I_0(k_1 a)}{I_1(k_1 a)}\frac{(2-\vartheta_1^2)^2}{(1-\vartheta_2^2)^{1/2}} \end{aligned} \tag{3.36}$$

This was then solved with the numerical function `fsolve` from the Optimization toolbox in Matlab using the code given in Appendix B.2.

Figure 3.4 shows the phase velocity ratio $\frac{v_p}{\beta}$ as a function of $\frac{\Lambda}{D}$ for two values of Poisson's ratio. These were chosen to show how little the phase velocity changes for the average values of Poisson's ratio for stainless steel. The phase velocity increases with increasing wavelength until it reaches the shear wave velocity β. This is called

the cut-off wavelength, Λ_c. M.A. Biot [3] comments on the behaviour of the phase velocity that the cylindrical symmetry allows for circumferential stresses which causes an "increase of rigidity of the material. (...) [rigidity] becomes greater as the wavelength increases, that is, as the depth at which the surface waves are felt becomes larger. (...) increase of rigidity causes an increasing value of the phase velocity." He further points out that this increase cannot continue beyond the shear wave speed as such a great velocity will induce shear wave radiation and decrease the energy of the Rayleigh surface waves. The cut off is partly due to imaginary solutions of $(1 - \vartheta_2^2)^{1/2}$, which should be real, in Eq. 3.36. For $\nu = 0.29$, Λ_c is approximately $0.495 * D$. With a radius of 4 mm, $\Lambda_c = 3.96mm$.

Even though this formula was derived for cavities in [3], the dispersion relation is assumed to be similar for the Rayleigh surface wave propagation on the exterior walls of solid cylinders. However, the wavelength should be less than the radius of the cylinder, or else waves from opposite sides will interact with each other and Λ_c does not follow the relationship above. For Rayleigh surface waves, the penetration depth[2] is given by equation 3.37

$$d_{e^{-1}} = 0.4\Lambda. \tag{3.37}$$

From Figure 3.4 it is apparent that for most stainless steel types, the Rayleigh wave speed does not vary much. The Poisson ratio for stainless steel varies between 0.28 – 0.35, depending on the process and composition. The low variance in wave speed makes it possible to assume that a frequency chosen for one specific Poisson ratio of stainless steel will work for other ratios in the aforementioned range.

However, the Poisson ratio assumes stable, isotropic, linear elastic material. During production of the dampers, they may have been exposed to different temperatures and environmental conditions. Together with random pore irregularities from processing and other faults which may have come from knocks during transportation/assembly/storing, the material is not likely to be homogeneous or isotropic [4, p.180].

3.2 Signal Propagation

So far, only transmitting a signal has been investigated (Section 2.1.1). Receiving a signal uses the same principle, only reversed. The simplest way to create the coil necessary for generation/receiving is using flexible PCBs, which is also how Techni has implemented their existing system. As described by [15], five-layer PCBs are typical.

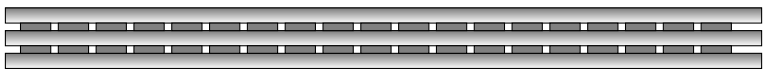

Figure 3.5: Cross-section of five-layer PCB.

[2]The depth of which the amplitude of the wave has decreased to e^{-1} of its original value [22, p.136]

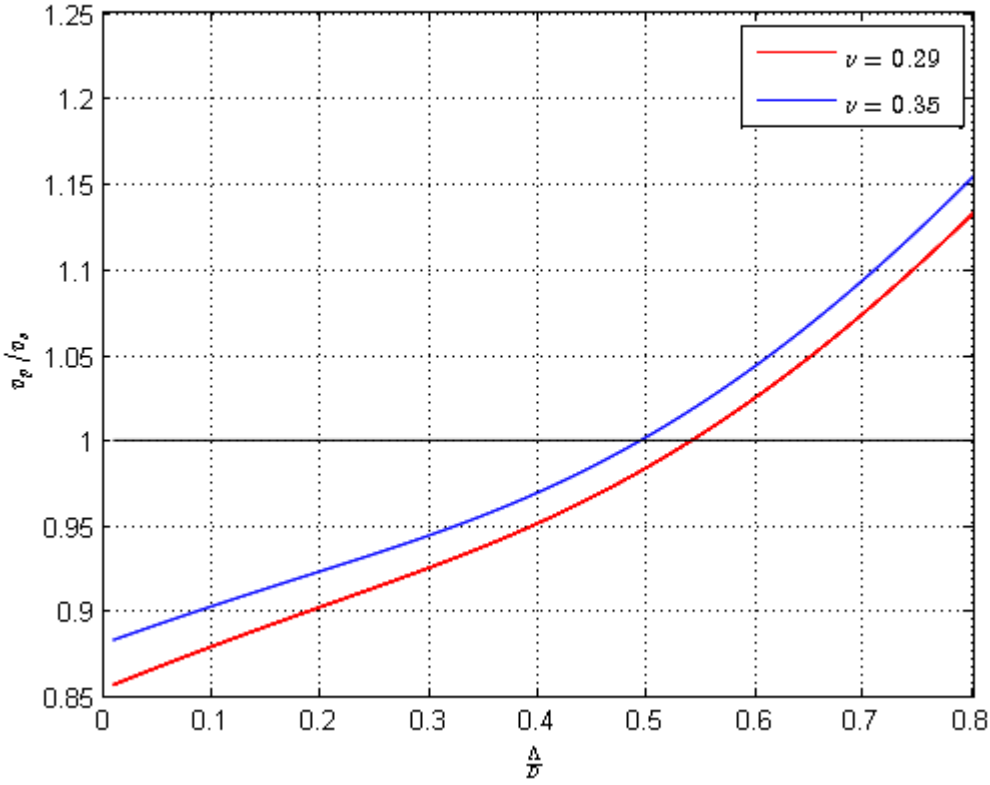

Figure 3.4: Plot of phase velocity of Rayleigh surface waves for two values of Poisson's ratio. The phase velocity has been normalized with respect to the shear wave velocity in stainless steel for $\nu = 0.29$.

In Figure 3.5 the transmitting and receiving coil are seperated by a PCB layer. This is convenient because the transmitting and receiving coil often require different impedance matching networks.

Impedance matching is an important part in EMATs design to increase SNR. Simple matching networks may be created with transmission lines, integrated chip components or lumped components, depending on the size and technology available. The frequency chosen determines both the matching networks and the coil spacing, which means that most EMATs have a narrow working frequency band of high quality.

A continuous signal would drown any reflections, so a pulse is used to measure the distance. A problem that arises with pulses is achieving a strong signal with high temporal resolution. Different coils may be used to generate a Rayleigh wave, such as a racetrack coil or a meander coil. A meander coil will give a high amplitude, but a poor temporal resolution. An approach to solving the problem of resolution is using a chirped signal (approach 1) or creating the meander coil with seperate exciters and amplifiers for each turn (approach 2). For approach 1, the meander coil is modeled as a chirp, where the spacing decreases to the chosen excitation wavelength over the width of the coil. The advantage of this approach is that the echoed signal will have this exact unique waveform, and the receiving coil should have the reverse chirp configuration (because of reflection). The signal may be pulsed or continuous. See Figure 3.6 for transmission diagram.

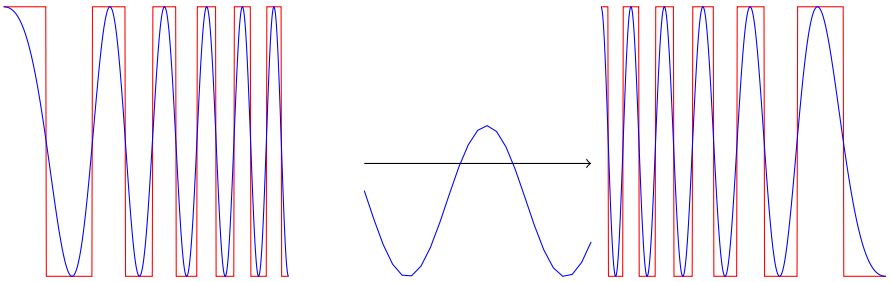

Figure 3.6: Figure of chirped signal excitation and receivement. The color red signifies the coil, while blue is the signal.

Approach 1 is advantageous because of its simplicity, and that it does not require extra electronics. For the second approach, a more complex design of the coil is required. By placing separate amplifiers and signal inputs at each turn of the coil, the directionality of the pulse will be controlled, as shown in Figure 3.8. As with approach 1, the signal may be customized to be continuous or pulsed.

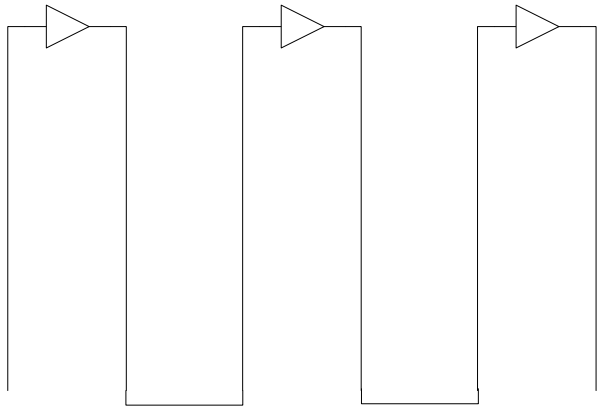

Figure 3.7: Coil design with separate amplifiers.

The signal propagation in the negative z-direction is not amplified by the following turns, causing the signal returned to the receiver to be much smaller than the one which is reflected off the edge of the piston in the positive z-direction. To produce a signal in the opposite direction, the pulse generation should start in the opposite end. A disadvantage with this approach is the problem of amplifier saturation. The amplifiers of the receiving coil must be configured so that the pulse has left the transmitting coil before they are open for detecting the reflected signal.

3.2.1 Crosscorrelation

For either of the two approaches described above, the output signal which the receiver picks up will be distorted by noise. The simplest way to identify the reflected signal in the output signal is by using a crosscorrelation function [24, p.116].

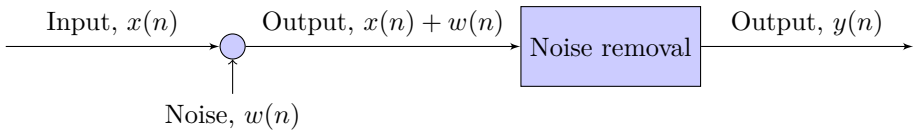

Figure 3.9: Signal flow through system.

Crosscorrelation describes how a sample value is similar to the other samples in the same period T, following Eq. 3.38. T denotes the period in which the signal is observed, and its maximum value is defined at $\tau = 0$. If $R_{xy}(\tau) = 0$, the functions are uncorrelated or statistically independent of each other.

$$R_{xy}(\tau) = \lim_{T\to\infty} \frac{1}{t} \int_{-T}^{T} x(\tau)y(t+\tau)\,\mathrm{d}\tau \tag{3.38}$$

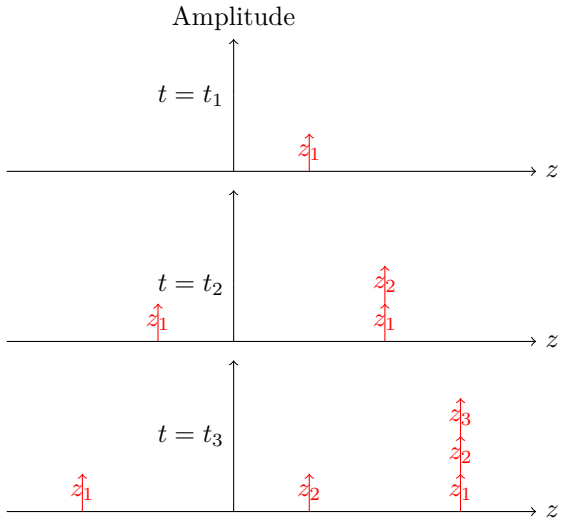

Figure 3.8: Signal diagram of complicated coil with three turns. Snapshots in time. Positive z-direction: Top picture shows the excited signals at time $t = t_1$, when the first turn only is active. At time $t = t_2$, turn no.2 excites an equal signal which is added to the first signal's amplitude. At time $t = t_3$, turn no.3 excites a third signal which is added to the two previous signals' amplitudes.

A simple Gaussian pulse, Eq. 3.39 has been used to exemplify an impulse function entering the system, Figure 3.10, left. The output signal before noise removal, Figure 3.11, left, contains both the white noise and the signal. Following an autocorrelation, the noisy output signal is reduced to the same Gaussian pulse as the input, Figure 3.11 right.

$$f(x) = a \exp\left(\frac{-(x-b)^2}{2c^2}\right) \tag{3.39}$$

where $a = \frac{1}{c\sqrt{(2\pi)}}$ denotes the amplitude, b the center point and c the Full Width at Half Maximum (FWHM) of the function. The values of a, b and c are chosen so that the pulse fulfills the requirements for a probability density function with expected value $\mu = b$ and variance $\sigma^2 = c^2$.

Creating a more unique pulse than a gaussian pulse, e.g. a gaussian modulated sine pulse with odd symmetry, will give this method an even greater success rate. Some reflections and echoes in the damper system may have a similar waveform to the simple gaussian pulse, and adding a more complicated pulse with odd symmetry with heighten the chances of identifying it as the incoming signal.

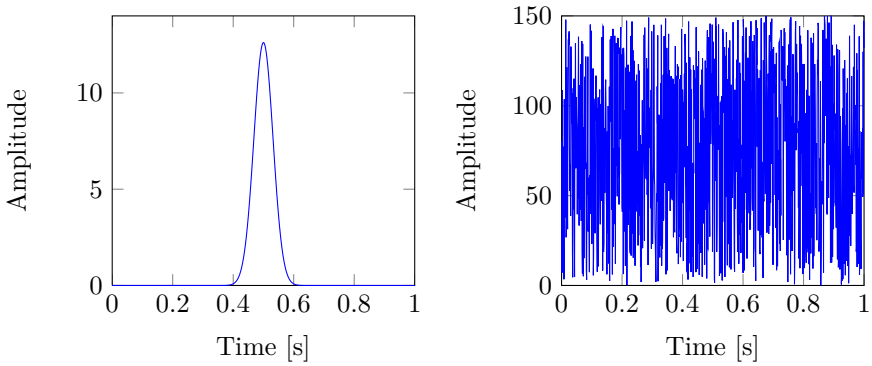

Figure 3.10: Signals entering the system. Left: Gaussian pulse $x(n)$, right: white noise $w(n)$.

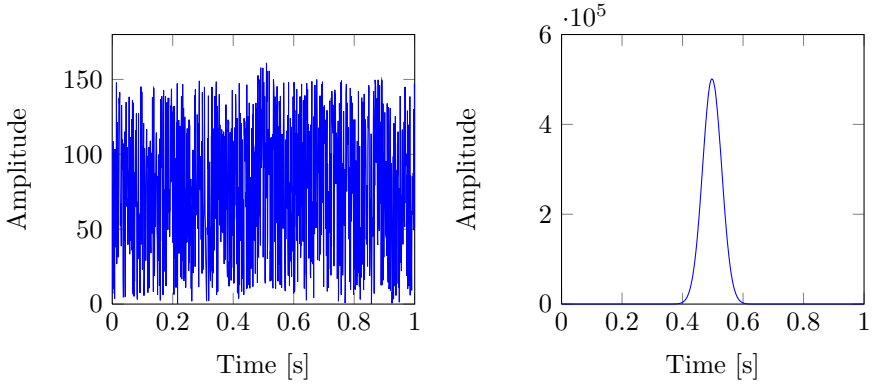

Figure 3.11: Signals exiting the system. Left: Output signal before noise removal $y(n) = x(n) + w(n)$, right: output signal after crosscorrelation $R_{xy}(n)$.

3.2.2 Data Acquisition System

Revolve has developed a Data Acquisition System (DAS) which has a multitude of inputs and outputs that collect data from the various sensors in the racing car. It is reasonable to assume that this is standard in most vehicles, and that the signal types are standarized. The two most common signal types are analog signals (0 – 5 V) and CANbus. Because of the signal processing that will/must take place with this damper system, CANbus is a reasonable choice for avoiding extra conversion between analog and digital signals.

In order to compensate for the irregularities associated with production, and the inhomogeneity of the steel, the sensor should be calibrated when mounted with respect to wave speed. This can be done by having a "calibrate" button in which the sensor is mounted on the damper at a distance of e.g. 10 cm. If the sensor is used as a part of a larger DAS, (which is the case for Revolve), a series of calibrating measurements should be done and a calibration table will be set up in the data acquisition system.

3.3 Existing Model and Test Data

Techni AS has an EMAT optimized for larger cylinders. The aim of this is to monitor, and at a later stage control, the movement of pistons in industrial applications. For this to be possible, the sensor must be very low-maintenance and survive harsh conditions such as off-shore environments. The model and test data for this configuration will be described here.

3.3.1 Setup

In order to test the EMAT sensor system, a test bench was set up as depicted in Figure 3.12. The aim of setting up this test bench was to establish accuracy and repeatability of the measurements.

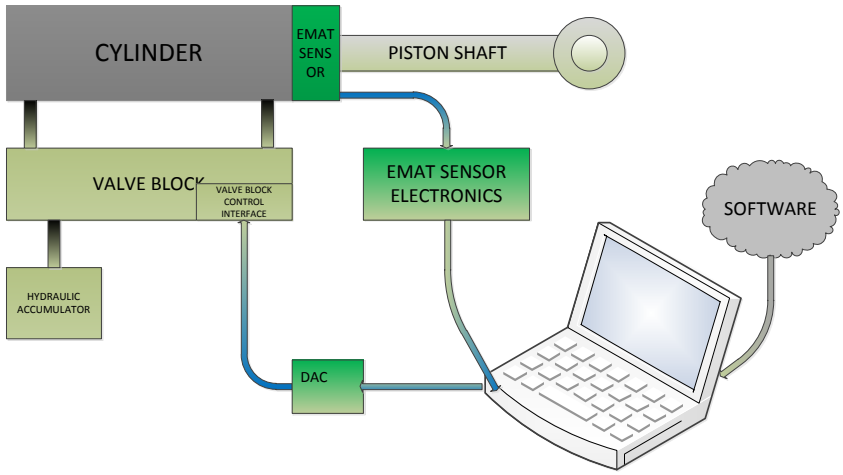

Figure 3.12: EMAT sensor verification setup from Techni AS.

To ensure accurate measurements, care was taken to fix all elements of the test bench so that there was no unwanted movement. The measurements were all performed against a reference system using a mechanical ruler of at least 1 mm accuracy fixed on the piston shaft.

3.3.2 Measurement Setup

The measurements were performed using the following procedure.

1. Move the leading edge of the reflective part (such as the eye of the rod) to the desired position referenced by the ruler.
2. Configure software to transmit and record a set of bursts. Should use at least 50 measurements.
3. Perform readings.
4. Record reference position.
5. Compute mean and standard deviations for each measurement.
6. Compare measured data to reference position.

3.3.3 Actual Setup

Due to in-house problems, the desired setup as depicted in figure 3.12 has not been completed. The modified setup is given in figure 3.13, where the hydraulic control of the piston is removed, and an external wave source is used.

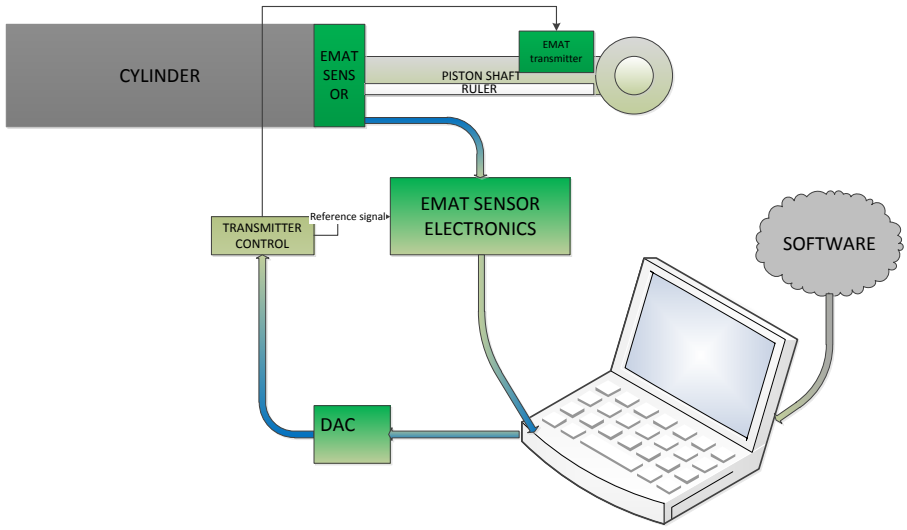

Figure 3.13: Actual EMAT sensor verification setup from Techni AS with seperate transmitting module.

Because of the change in setup, the background given in chapter 2 is not accurate, but the transmitting module is assumed to give close to the same waveform as the EMAT sensor. Because of the short wavelength, the waves are assumed to be plane waves close to the propagation direction, as shown in figure 3.14.

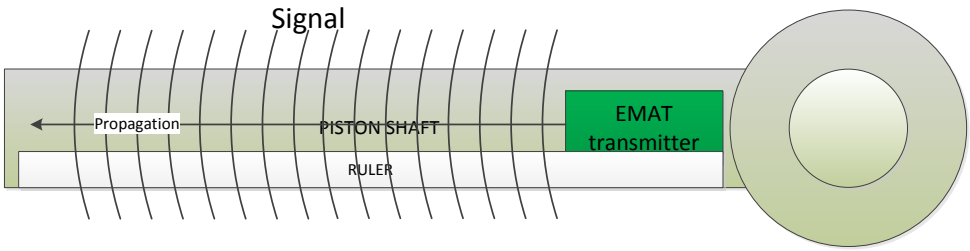

Figure 3.14: Wave propagation on piston shaft with external transmitter

Signal

There are various problems associated with this setup, as the transmitter will excite a wave in both forward and backward direction. Various effects may cause unwanted reflections which give false positives:

- An echo from opposite end of the rod (where the eye is attached)
- Reflections from flaws on the piston shaft such as scratches which may have occured during production or in use
- Multimode propagation with different propagation velocities if excited mode is not controlled

Additionally, the signal will be very weak and noisy. To find the correct reflection amongst all the noise, crosscorrelation is employed with the transmitted signal, as described earlier. Further, the EMAT antenna is configured such that reflected echoes are attenuated. This was explained in section 3.2.

Using a configured transmitted signal, it is possible to detect the reflection and determine the distance travelled by the wave in ideal conditions. As this is in-house testing, the additional knocking of the piston in real life has not been accounted for or tested prior to the thesis.

3.3.4 Measurements Statistics

Some measurements were performed in order to determine the precision of the setup. Figure 3.15 shows that there is no apparent relationship between the distance of measurement and the discrepancy. This then supports the assumption that the Rayleigh surface wave is not significantly attenuated for this setup.

Apart from measurements near 57 mm and 75 mm the discrepancy is close to 10% or less, shown in Figure 3.16. This is not satisfactory for a finished product, where the discrepancy should be less than a mm. The discrepancies may have been caused by several effects:

Sampling frequency If the detector is a little bit off when it comes to sampling the reflected wave, this will yield an error.

Reference measurement The reference measurement was made by visual estimate from a ruler placed by the same person.

Coil imperfection There might be imperfections both in the receiving coil and excitation coil which are not accounted for in the signal processing algorithms.

Amplifier saturation Because the EMAT excites longitudinal modes as well as the main Rayleigh mode, these will reach the receiver first. Even though the receiver is not configured to pick up these signals, the amplifiers may be saturated from detecting them when the Rayleigh mode arrives.

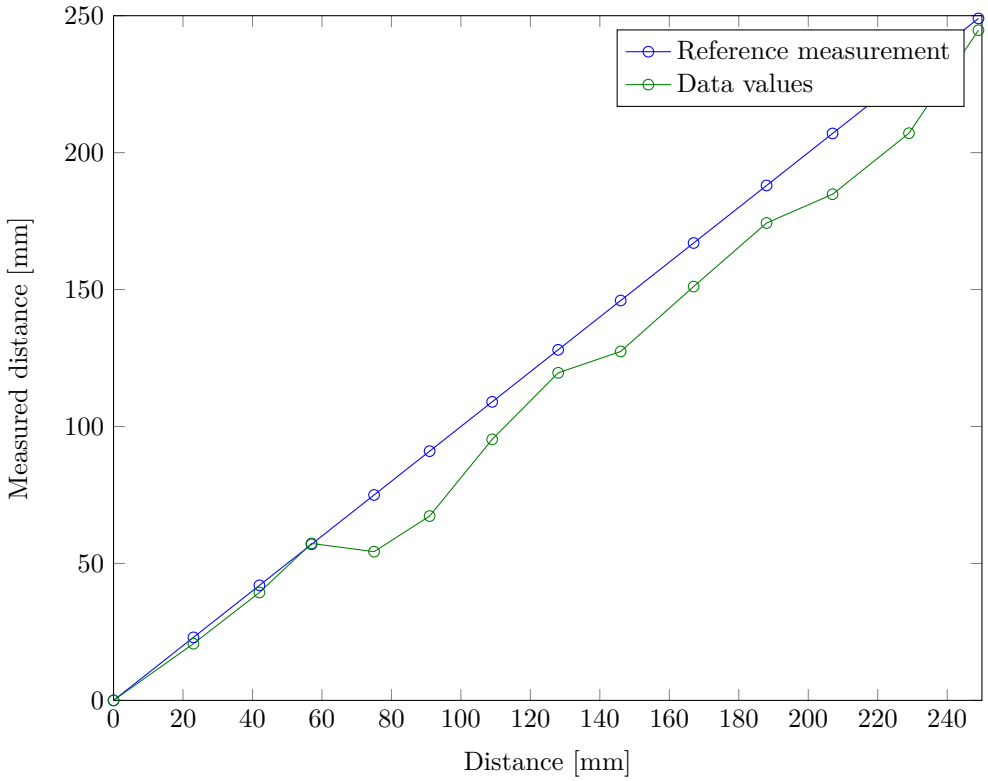

Figure 3.15: Measurements performed March 5th 2012. Some inaccuracy may be found in the reference measurement as these were done using a mm-ruler. Green: measurements, blue: reference (ruler).

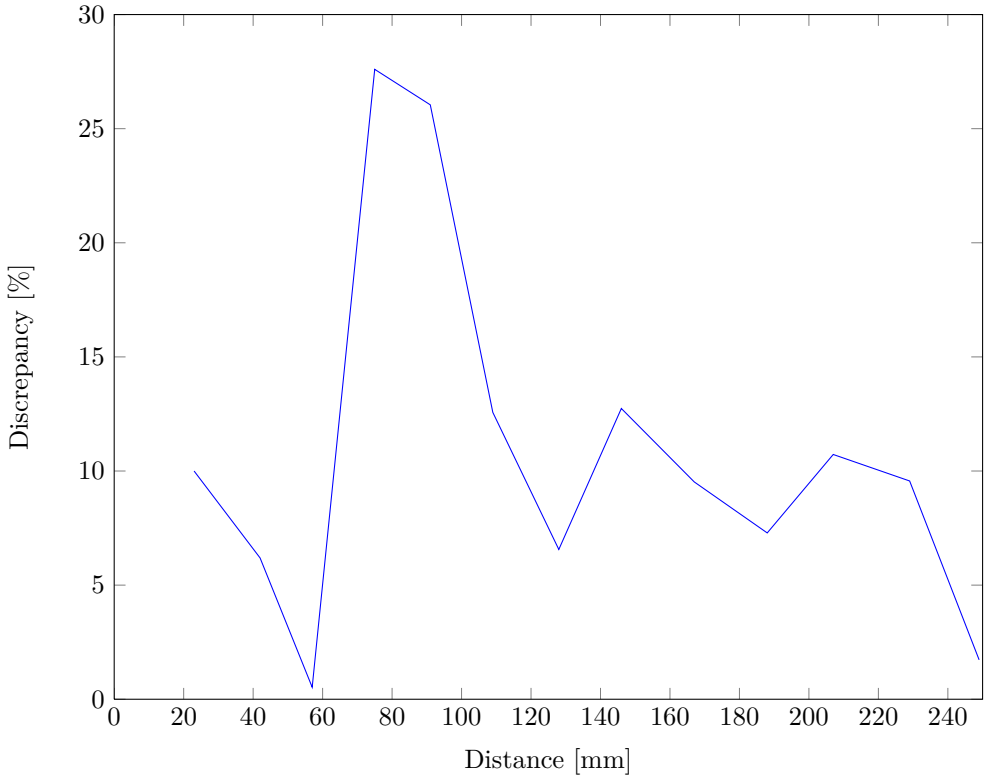

Figure 3.16: Discrepancy of measurements from March 5th 2012.

Signal in an Actual Piston

The signal in a realistic piston will be subject to both internal forces in the piston (normal movement and twists), and external forces (waves, rain, strong winds). The behavior of the signal during these forces must be tested so that alterations to signal processing and antenna type may be performed before final production. Because the electronics were not finalized or encapsuled, it was not possible to perform these types of tests. However, basic testing with touching the piston during sampling was performed and no differences in signal were detected – the distance measured was constant.

Chapter 4

Method

The new damper sensor and evaluation of positions and mounting difficulty is given in Section 4.1. Section 4.2 describes FEM which is used to analyze the wave problem. Section 4.2.1 introduces the various physics nodes in COMSOL Multiphysics which is the FEM software used in the thesis. The following sections present and discuss the results from simulations. The simulations were performed in 2D axisymmetric geometry. This greatly reduced the simulation time from a 3D problem.

All axes in figures from COMSOL Multiphysics are in [mm] if nothing else is specified.

4.1 New Damper Sensor

In the process of synthesizing a solution for implementing EMAT as a damper position sensor, various positions were considered. The working concept is given in Figure 4.1, while the other solutions are given in Appendix D.

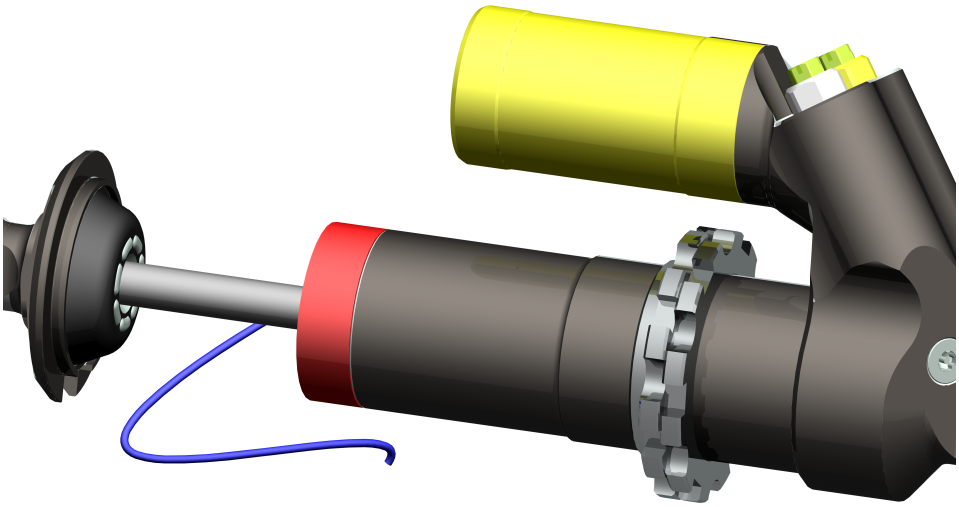

Figure 4.1: Working concept, pos1. Red=EMAT, blue=cable. Sensor size: outer diameter=32.6 mm, inner diameter=10 mm (1 mm liftoff), thickness=10 mm.

pos1 This is considered the ultimate position for large applications in which Techni AS already has a product. The sensor is mounted with an adhesive on the bottom face of the main cylinder. The cable which is connected to the coil would have to be guided through the spring somehow, without damaging the movement of the damper. See Figure 4.1.

pos2 Similar to pos1, but mounted on the bottom face of the damper. The disadvantage with this position is the bumpstop. The bumpstop is supposed to protect the damper from damage during hard piston movements. As with pos1, the coil guiding is also a problem. See Figure D.1.

pos3 A suggestion which avoids the moving spring, but complicates the design because of the coil position/placement. It is difficult to guide the cable from the interior of the cylinder to the exterior, see Figure D.2. Figure pos3 holds for positioning the sensor both as the "compression shims", and as the blue bumpstop shown near the "rebound shims" in figure C.1.

pos2.5 At the end of the thesis work, a new placement of the EMAT sensor had to be considered because of the change in damper movement. This new position is given in Figure 4.2, with a close-up in Figure 4.3. The advantage of choosing this configuration is the possibility of directing the cable through an opening in the bottom of the damper, which is meant to ease the removal of spring. As shown in the close-up, the EMAT should be configured so that it is a part of the bottom bumpstop (marked red in Appendix C).

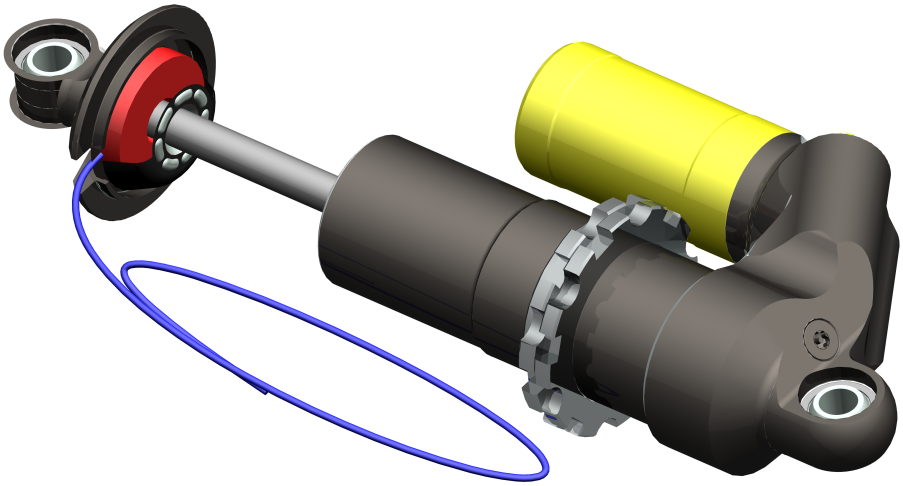

Figure 4.2: pos2-5. Red=EMAT, blue=cable. Sensor size: outer diameter=28 mm, inner diameter=10 mm (1 mm liftoff), thickness=5 mm.

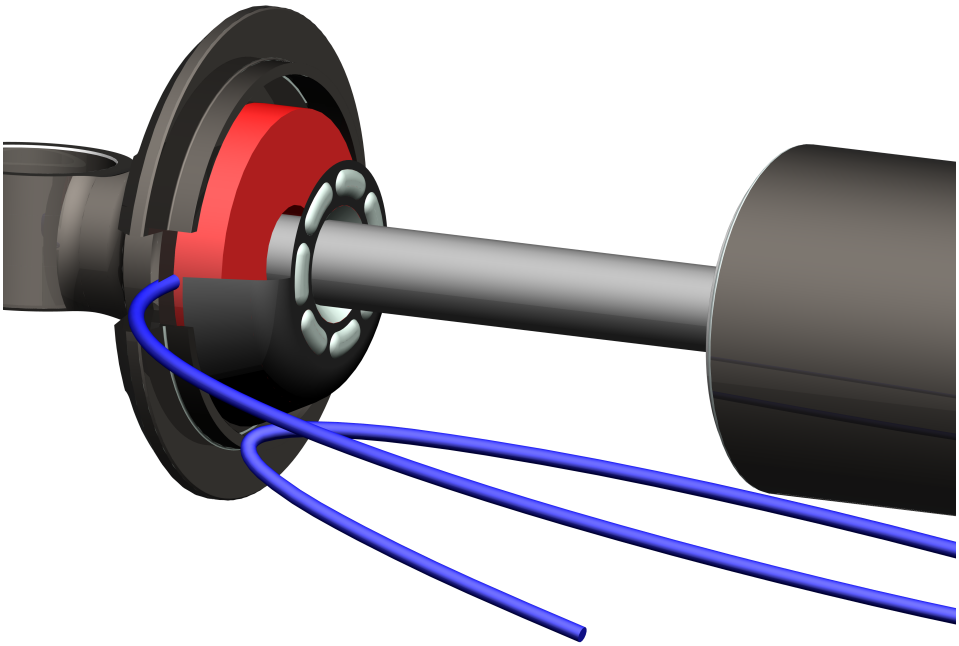

Figure 4.3: Close-up of position 2.5 for damper sensor.

4.2 Finite Element Modeling

FEM is used in the thesis for modeling the excitation and transmission of Rayleigh surface waves. The method divides the object of interest into several elements which are then analyzed seperately before the solution is given for the whole object. The strength lies in the possibility of performing calculations on complicated geometric figures. Additionally, it is easy to perform multiphysics calculations using FEM as the same element may have multiple equations — one for each physics environment. The main drawback is the time needed for calculation, the smaller elements, the longer the computational time. Open-air problems or radiative problems cannot be solved "as-is", because the geometry must be finite. This may be compensated for using special layers to emulate infinity. Finite Element Method also requires the user to have good knowledge of the physics behind the problem, as it will give an answer regardless of whether its physical or not. FEM follows a simple algorithm to perform calculations:

- Divide the object into small building blocks of simple geometry (called meshing).
- Give each building block the properties of the physics in question by a polynomial with unknown coefficients.
- Create a system of equations by recognizing the nodes combining the elements.
- Solve the system of equations and calculate the unknown parameters in the physics equation of the object.

In addition to choosing the type and size of elements, the number of nodes on each element may vary. There will always be a node at the corner of each element, and often additional nodes at the midpoint of the branches connecting them.

4.2.1 COMSOL Multiphysics

COMSOL Multiphysics, formerly FEMLAB, may be used to model and simulate multiphysics systems. It was chosen for the thesis because of previous knowledge of modeling with this software, and the availability at Techni AS. The software offers several tutorials in the different physics environments, but none for EMAT. A model provided by the company has been used as inspiration.

COMSOL solves the FEM problem by the use of a weighted residual formulation to transform the differential equations into integral equations. The specific method implemented is called the Galerkin method, where the weighted residuals are equal to the unknown functions mentioned above.

Below follows a list of the most important nodes used for modeling the EMAT.

Global Nodes

Perfectly Matched Layers PMLs are used as an absorbing layer to decrease the regions in a FEM model to save computational powers. They are called "perfectly matched" because the interface between the PML and non-PML does not reflect any of the incoming wave, which would happen with a normal absorbing medium. PML domains cannot be a part of the physics modules, and are defined in the main geometry section under *Definitions*. COMSOL has implemented Perfectly Matched Layer (PML) for the Solid Mechanics physics using the following formula to transform a general coordinate t.

$$t' = \frac{t}{\Delta_w}^{n}(1-i)\Lambda F \tag{4.1}$$

where Δ_w is the width of the PML region, and is automatically detected by the system as together with the coordinate. The scaling factor F and the order n may be specified in the PML node. They are by default set to unity. Λ, the wavelength, is defined by the physics, or may be user-defined in the PML node.

Mesh The mesh node specifies the number of elements the domains/volumes consist of. Optimizing this node can save a lot of computational power, as more elements increases the computational time. A rule of thumb specifies number of elements per wavelength in acoustic simulations to be 5 or 6. The number of elements should be increased for areas where there are rapid changes, and decreased in areas where no big changes are expected to minimize computation time.

Solid Mechanics

Body Load Body Loads are used to "receive" forces such as gravity or here; the Lorentz force. The components of the force can be specified for each direction as single force components or sum of force components. For the interaction between the Solid Mechanics physics and Magnetic Fields physics, the body load domain needs to be a part of both physics. The equation for a time dependent simulation is given in eq. 4.2, where $\vec{u}$ is the particle displacement, σ the conductivity, and $\vec{F}$ the force. The Lorentz force is accessed by the body load with the function `mf.FLtzr`.

$$\rho\frac{\partial^2\vec{u}}{\partial t^2} - \nabla\cdot\sigma = \vec{F}v \tag{4.2}$$

Fixed Constraint Fixed Constraints are used on edges of geometries to emulate a constraint for which the displacement is equal to zero in all directions from this boundary.

Magnetic Fields

Ampère's Law This node is a default node for the Magnetic Fields physics. It adds the law to the physics node, and defines the constitutive relation and other physical properties associated with Ampère's Law. The equation governing the physics is given below.

$$\sigma \frac{\partial \vec{A}}{\partial t} + \nabla \times \left(\frac{\vec{B}}{\mu_0 \mu_r} \right) - \sigma \vec{v} \times \vec{B} = \vec{J} \tag{4.3}$$

External Current Density In order to get a current-carrying wire, the External Current Density node is employed to the specified domain(s). The current (given in A/m^2) may be specified as a constant value or a function of e.g. time which may be defined for the whole model. The current density follows the same equation as Ampère's Law, given in eq. 4.3.

Magnetic Insulation For the Magnetic Fields physics, the default boundary condition is Magnetic Insulation. All boundaries of which is active for this condition causes the normal component of the magnetic field to be zero.

Magnetic Flux Conservation The permanent magnet used during modeling has its magnetic potential defined by this node. Since the magnet is permanent, it applies a stationary equation (eq. 4.4) and the magnetic field is calculated from the specifed remanent flux density.

$$\nabla \cdot \left(\mu_0 \mu_r \vec{H}_{ME} \right) = 0 \tag{4.4}$$

4.2.2 Materials

The materials chosen for the different parts of the EMAT system are the following

Stainless Steel It is assumed that the piston rod is composed of stainless steel with the following material parameters: **density** $\rho = 8000 kg/m^3$**, poisson's ratio** $\nu = 0.29$**, Lamé's first parameter** $\lambda = 118.76 GPa$**, shear modulus** $\mu = 86 GPa$**, relative permeability** $\mu_r = 1.008$ **and conductivity** $\sigma = 1.3889 S/m$**.**

Air All surrounding space is modeled as air, with relative permeability and permittivity of unity.

Neodymium magnet The rare-earth material is chosen as the permanent magnet surrounding the meander coil and providing the static magnetic field. It is chosen because of its high coercivity and high magnetization. Neodymium magnets are commonly used in hard disks, tools and other industrial applications. The magnets have a lower curie temperature than Sm-Co magnets, but are much stronger (higher flexural, compressive and tensile strength). They are often produced by sintering, but this increases corrosion and protective layers (such as nickel or copper) may be employed [2]. It is important to take

care when handling such strong magnets, the sintering process makes them vulnerable to cracking in small, sharp pieces. Additionally, fine mechanics will be ruined by the strong magnetic field. Neodymium magnets are characterized by: **remanence** ($M_r = 1.3T$)**, coercivity** ($H_{ci} = 750to200kA/m$)**, curie temparature** ($T_c = 583.13K$)**.**

4.3 Modeling Eddy Current and Magnetic Flux Density Penetration in Stainless Steel

In order to investigate the eddy current excitation and the magnetic flux density, the built-in model "Eddy Currents in a Cylinder" included with COMSOL Multiphysics 4.2a was modified and simulations were performed with changes in frequency and the spacing between the conductive surface and the coil. In [25] the validity of the well-known Dodd and Deeds [8] model for eddy currents using COMSOL was tested. Ribichini [25] concluded that the two models have excellent agreement, thus validating COMSOL's ability to model eddy currents properly.

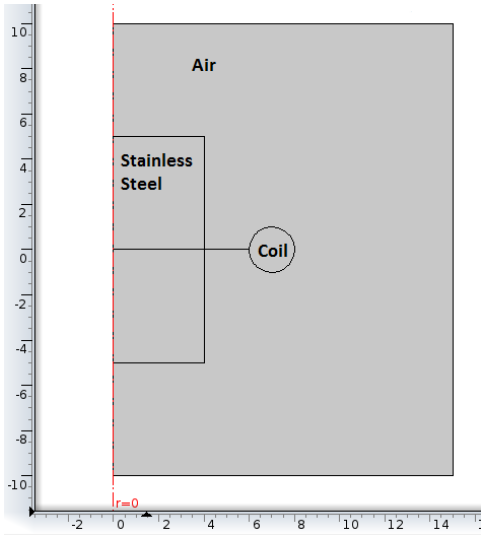

Figure 4.4: Model in COMSOL.

Due to 2D axisymmetric geometry, the computation time is reduced from 3D modeling and no special care was taken to refine mesh size. The meshing was chosen to *Fine triangular mesh* controlled by the physics chosen.

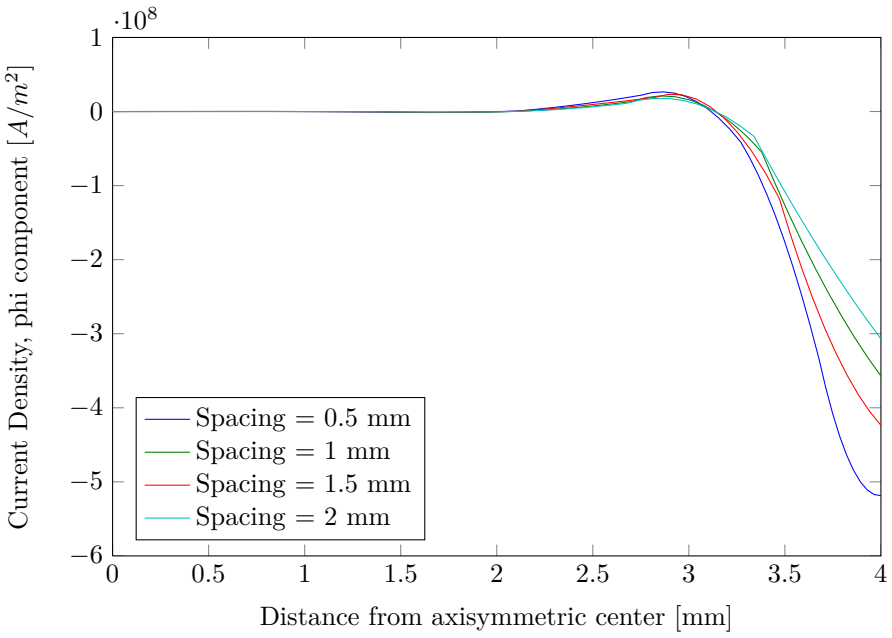

Figure 4.5: Eddy current density for different values of spacing at 1.5 MHz.

4.3.1 Eddy Current Changes

The eddy current density did not change noteworthy for the spacing sweep, as may be seen in Figure 4.5. The same may be seen in Figure E.2 for 2.5 MHz.

When changing the frequency, the same trend may be detected. This is shown in Figure 4.6. Comparing this with the figure showing the eddy current skin depth dependence in Figure 2.1, for 2 MHz the skin depth is 0.31 mm in the latter. This corresponds well as shown in Figure 4.7. With the supporting analysis provided in [25], it is assumed that COMSOL models eddy currents precisely, as both the simple formula of calculating skin depth for eddy currents mentioned in Section 2.1 and the more complicated model from [8] agree with the simulation.

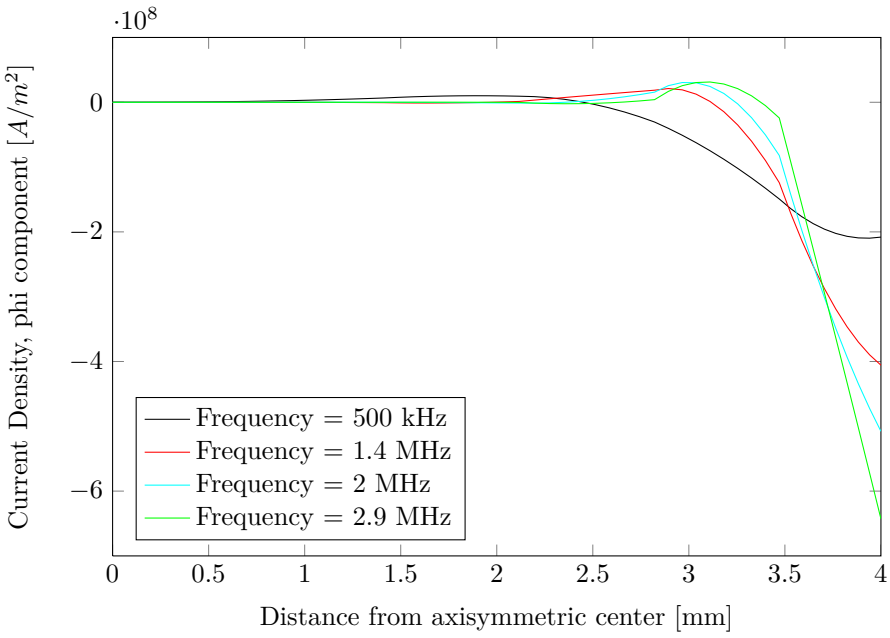

Figure 4.6: Eddy current density for various frequencies with 1 mm spacing.

4.3.2 Magnetic Flux Density Changes, Dynamic Field

The magnetic flux density decreases with approximately 50% when going from a spacing of 0.5 mm to a spacing of 2 mm, as may be seen in Figure 4.8. This is further supported for 2.5 MHz, which is shown in Figure E.3 in Appendix E.

This magnetic flux density is the dynamic field described in Eq. 2.7. It is then important to have the sensor mounted as close to the moving piston rod as possible, without restricting its movement. Some testing will have to be done to determine the spacing, as the piston rod may drift around its center of movement.

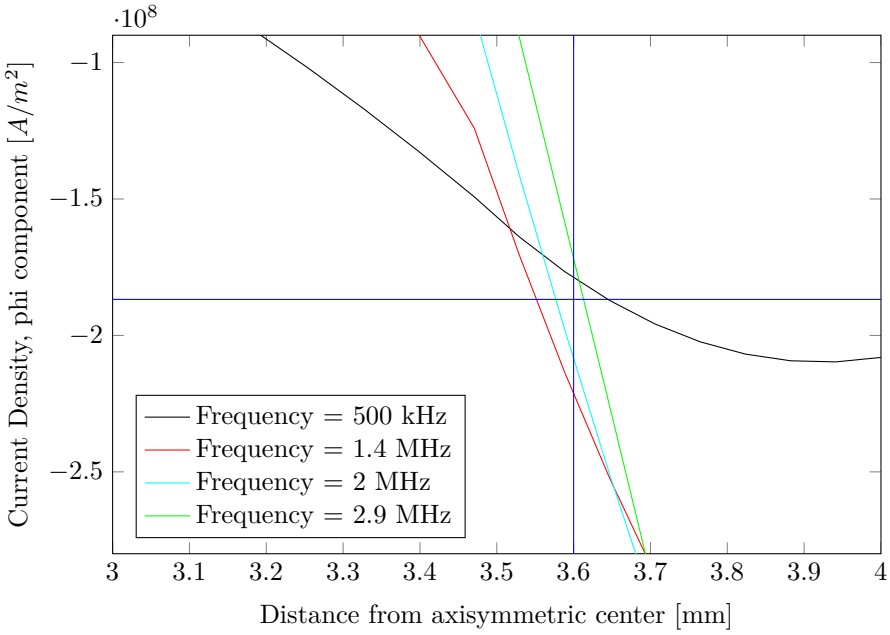

Figure 4.7: Eddy current density for different frequencies with 1 mm spacing. Blue horizontal line marks the skin depth calculated from the COMSOL simulation for 2 MHz, while blue vertical line marks the skin depth from Figure 2.1

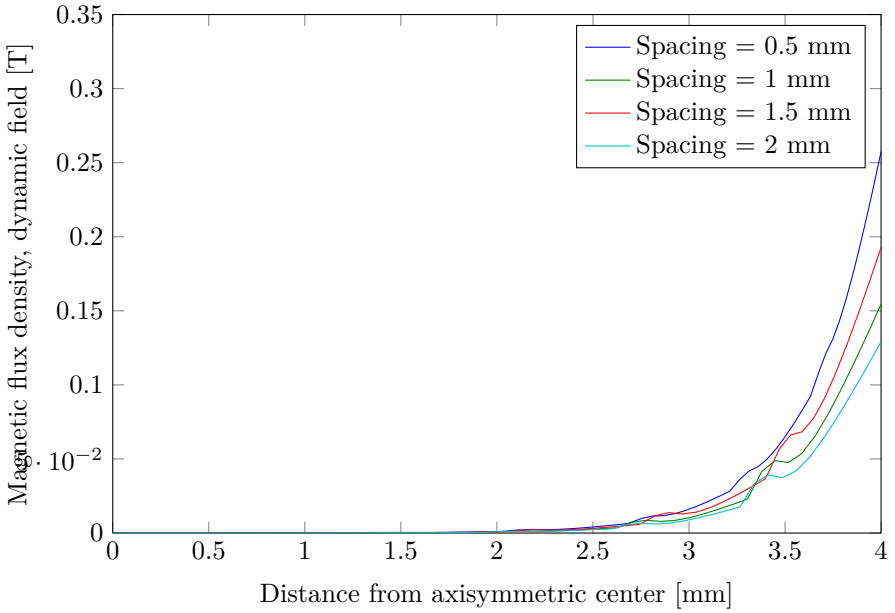

Figure 4.8: Magnetic flux density, dynamic field, for different values of spacing at 1.5 MHz.

4.3.3 Magnetic Flux density, Static Field

A different geometry of a simple quadratic block with sides of 10 mm surrounded by air, figure in Appendix E, was chosen to investigate the static magnetic field caused by the neodymium magnet.

When analyzing Figures 2.1, 4.5 and 4.8 it is logic to assume that a small spacing is desirable in order to have a high enough frequency to ensure that the Rayleigh wavelength is small enough to keep to the surface layers of the conductive surface. The dependence of spacing for the static magnetic field as depicted in Figure 4.9 is not crucial in comparison with the other parameters.

4.4 Modeling EMAT System

From Figure 3.4, the Rayleigh phase velocity is between 88% – 100% of the shear wave velocity. The shear wave velocity for stainless steel with the parameters mentioned is $v_s = \sqrt{\frac{\mu}{\rho}} = \sqrt{\frac{86GPa}{8000kg/m^3}} = 3279m/s$. With a radius of 4 mm, the wavelength, Λ_{min}, should be less than 2 mm. This gives a minimum frequency of $f_{min} = \frac{v_s}{\Lambda_{min}} = \frac{3279m/s}{2mm} = 1.64MHz$. However, due to technical difficulties associated with the computer provided for the simulations, they were performed for a frequency of $1MHz$. A higher frequency required a higher spatial and temporal resolution. COMSOL was not able to give realistic plots for frequencies where the

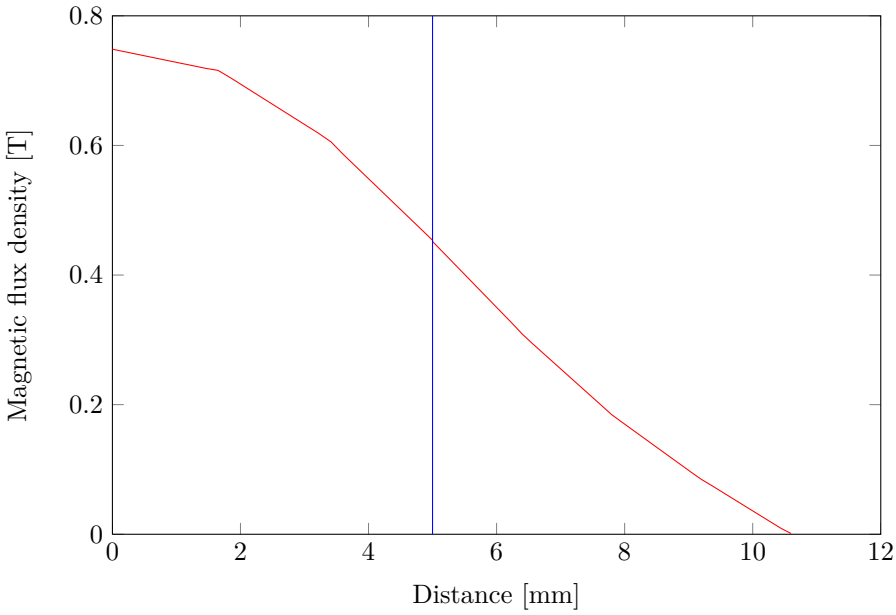

Figure 4.9: Static magnetic field strength as a function of distance from core of magnet. Magnet size: height=10 mm, depth=10 mm, width=10 mm. Blue vertical line indicates interface between magnet and air.

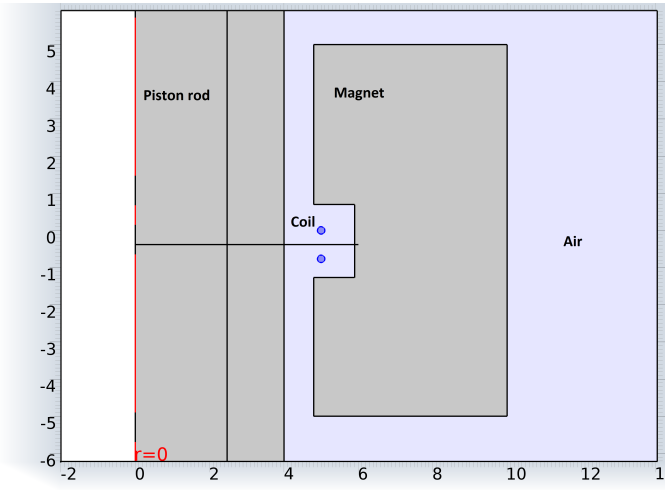

Figure 4.10: Geometry used for the full simulation of EMAT system. The spacing between the piston rod and magnet is 1 mm. The radius of the conducting coils is 0.1 mm, and their spacing is $\frac{\Lambda}{2}$. The magnet width is approximately 5 mm.

wavelength was greater than the radius because the penetration depth of the wave went beyond the axis of symmetry.

The geometries used for these simulations is given in Figures 4.10 and E.4. Figure 4.10 showed a large dependence on the magnetic field, so Figure E.4 was chosen for the subsequent simulations because it was close to what the EMAT would look like when produced.

Simulations with PMLs have not been performed because they required extra computing power. For future work, simulations should include both PMLs and boundaries representing the metallic face for reflection of wave.

The pulse in generated using a sine wave of frequency f. This is then pulsed using a rectangular window. The signal is given in figure 4.11 and described in Eq. 4.5.

$$Pulse(t) = \sin(ft) \times rect(t) \tag{4.5}$$

Transient Simulations

The transient response of the system was investigated using the "Time Dependent" study step in COMSOL. The times were configured as a range, *range(start_time, step_time, stop_time)*. This type of simulation is quite time-consuming. A short time step is necessary to avoid the numerical damping. The numerical attenuation may cause the pulse shape to be smoothed out while propagating [10].

The simulations were performed with a time-step of a nanosecond. Increasing the temporal resolution beyond this caused out-of-diskspace failure, as described in

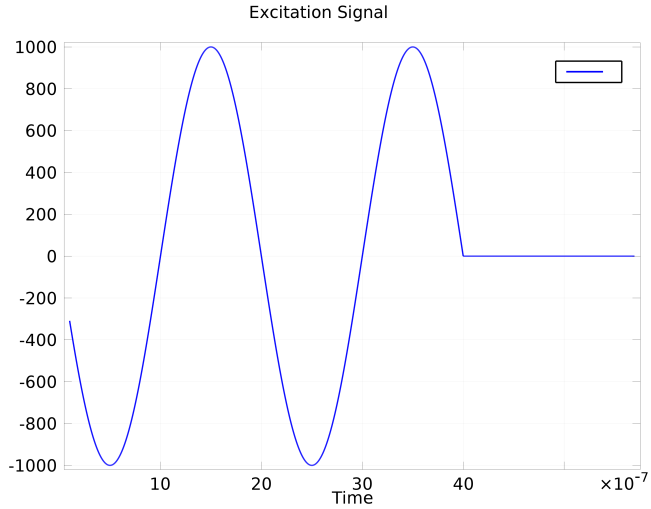

Figure 4.11: Excitation signal.

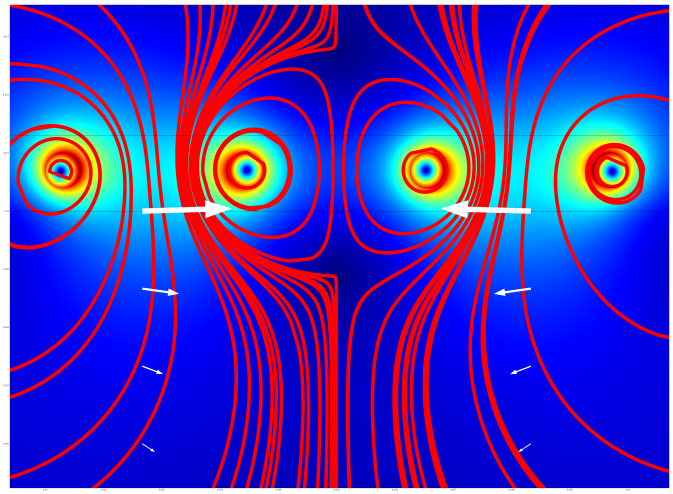

Figure 4.12: Lorentz force arrows in transient response. Red streamline: magnetic flux density. Surface: current density. Figure 4.10 altered with 4 coils instead of 2.

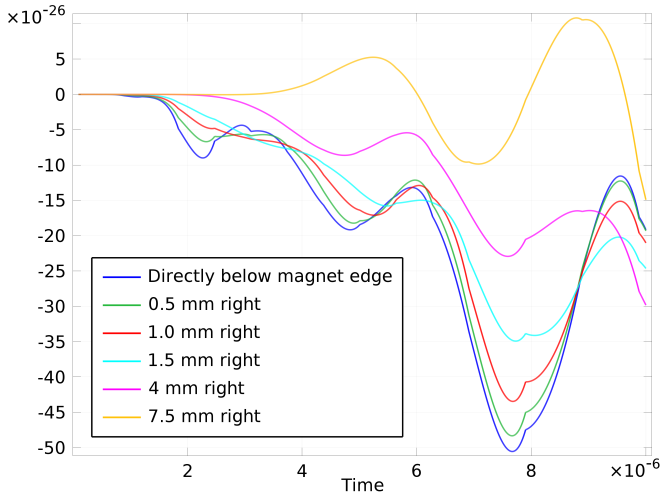

Figure 4.13: Displacement, vertical component [m].

the following section. However, the results produced with a nanosecond resolution was satisfactory, apart from an asymptote which appeared at multiple occasions. The trends and Lorentz force excitation were as expected.

As may be seen in Figures 4.14 and 4.13, the displacement field varies as a result of the excitation pulse. The following perturbations are caused by the mechanical displacement in the piston rod.

The highest amplitude of the Lorentz force may be seen nearest the magnet edge, and much smaller further away from the magnet, Figures 4.16 and 4.15. This is as expected since the Lorentz force acts as a result from both the magnetic fields and current field, from Eq. 2.7.

The vertical variation of Lorentz force did not vary that much for the first mm, as may be seen in Figures E.6 and E.5.

The asymptotic behaviour is evident in all figures, and reruns did not remove it. A possible cause of this behaviour may be that the time step is not small enough, and the changes in pulse are too great.

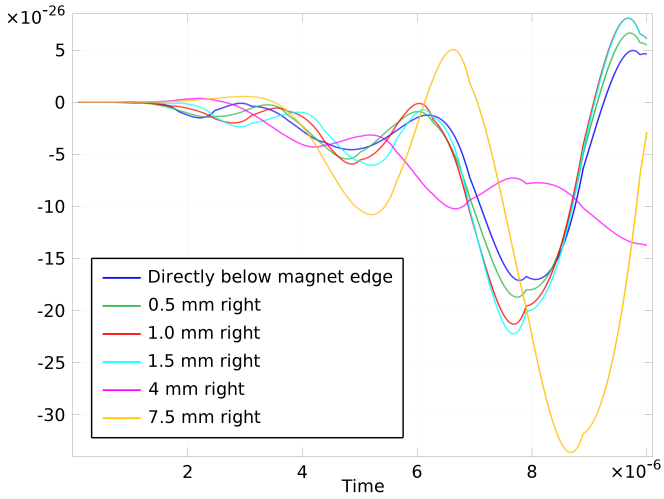

Figure 4.14: Displacement, horizontal component [m].

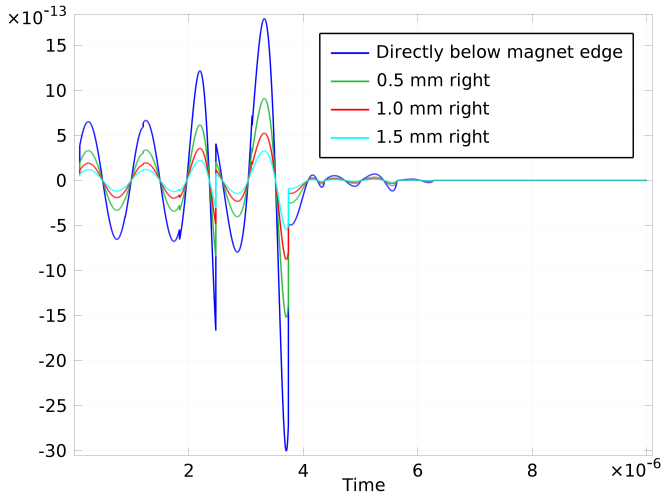

Figure 4.15: Lorentz force contributor, vertical component. The plot is given for horizontal points from magnet edge, amplitude in $[N/m^3]$.

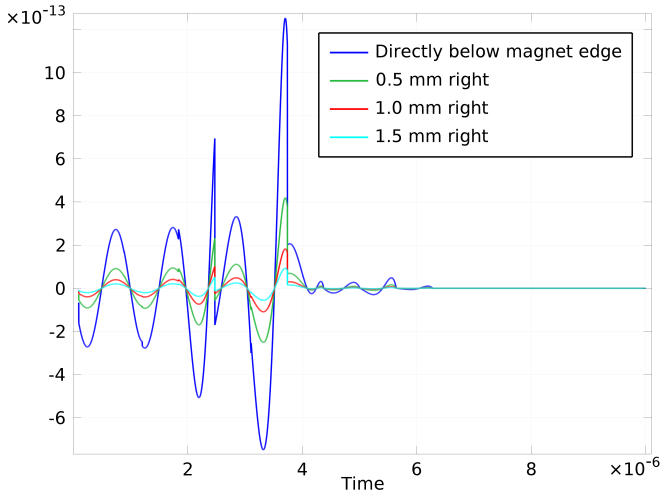

Figure 4.16: Lorentz force contributor, horizontal component. The plot is given for horizontal points from magnet edge, amplitude in $[N/m^3]$.

4.5 Technicalities

During the transient simulations, COMSOL stores-and-forwards the results on the memory before moving it to the harddisk. This is done to shorten the simulation time. However, when moving the results to the harddisk, it stores the results in raw format, which occupies a lot of space. This proved to be an issue when running transient simulations with high temporal resolution for a long time period. The computer set up for simulations had free space of 250 GB, but the simulations stopped halfway because it ran out of disk space. This was at the end of the thesis period, so this problem was not prioritized.

The meshing type ”Free Quad“ was used for the transient simulations do decrease the number of elements needed. This creates a quadrilateral mesh. The computer did not like fine meshes of the triangular type, and ran out of memory when the size of the elements were minimized, which is not necessary to the same degree with a quadrilateral mesh.

Chapter 5

Conclusion

The most significant advantages with EMATs are their ease of mounting and low-cost simple electronics. EMATs offer greater variation of modes than conventional piezoelectric transducers, and may survive in tougher environments. They have been used successfully in large industrial applications such as railway inspection and flaw detection in steel plates. Techni AS has developed a damper position sensor for use with large piston rods (wavelength $\ll$ radius).

Existing position sensors for Formula SAE dampers are based on resistivity measurements, where the manufacturer claims to have infinite resolution. The small size of the dampers makes it difficult to design an EMAT-based system.

Three different placements of the EMAT have been considered here, and one of them used as a working concept which matched Techni AS' recommendation. The design process for Revolve's racing car was not finished when the thesis work started. The following assumption was made at the beginning of this thesis: "The length of stroke of the dampers should be so small that it never reaches fully compressed position." However, through the course of the thesis and the design process of the racing car, this has changed. The dampers and spring set were thus configured to use the full length of stroke possible, making it undesirable to place a sensor in the working concept, position 1. Additionally, the problem of determining where the cable should be guided with a moving spring was not easy to solve. A possible solution to these problems is given in Section 5.1.

The configuration of the EMAT determined the wave mode, although both SH and Rayleigh were considered in the beginning. The dispersion characteristic of SH- and Rayleigh waves were investigated and plotted for the first few modes. Although the SH-waves exhibit no coupling to other modes, the configuration for distance inspection was not satisfactory with a 2-order magnitude drop over a distance increasement of 3x. The Rayleigh modes' non-dispersive character was derived and the validity of its velocity calculation discussed.

Choosing a meander coil design for which the SNR will be optimized was looked at with two approaches. The chirp approach offered a low-cost electronics advantage, while the amplified coil offered custom pulse configuration. A simple noise-removal algorithm using crosscorrelation between excitation pulse and output signal

was shown as this is the way Techni AS has configured their working system.

COMSOL Multiphysics offers a strong tool to solve problems where different physical environments are available. The validity of its results have been investigated for the forces and phenomena used by EMATs. COMSOL's capability of emulating the environments were in good agreement with analytical theory presented.

Technical difficulties were encountered with transient simulations because of limited diskspace and amount of memory.

The author feels that the position named 2.5 would be the optimal design as it allows for simple mounting and cable guiding without disturbing the movement of the dampers.

5.1 Future Work

Future work could include simulations with an EMAT covered by a bumpstop layer with the same characteristics as the existing bumpstop. Following this, experiments include validation of the parameters simulated, as well as testing with a racing car. Testing in a real racing environment would confirm/refute if

1. The dampers' movements are not hindered by the EMAT sensors.
2. The EMAT sensors are able to detect the distance despite the added noise of the cylinder striking the bumpstop.

Improving the signal quality beyond coil design has not been discussed in the thesis because it was beyond the scope of the project. The low SNR associated with EMATs is it main disadvantage and methods of improving the signal strength should be investigated. Dhayalan [7] discussed the use of ribbon MFCs placed between the coil and manget. His results for Rayleigh waves showed a doubling of signal amplitude both for simulations and experiments. This technique may easily be applied for EMAT sensors for FSAE dampers. The MFC can be less than a 0.5 mm, making them ideal for close-contact EMAT. A second study done by Jian et. al [17] supports the use of magnetic back-planes in his study of enhancement of EMAT with ferrite back-planes. The use of a ferrite back-plane requires a higher lift-off from the piston rod, which may cause a problem if the diameter of the magnet is reduced significantly. Because of the Formula SAE damper with spring, the maximum diameter of the magnet is limited.

Appendix A

Surface Rayleigh wave dispersion

A.1 Derivatives of the modified Bessel functions

$$\frac{\partial I_0(kr)}{\partial r} = -kI_1(kr)$$
$$\frac{\partial I_1(kr)}{\partial r} = -kI_0(kr) - \frac{I_1(kr)}{r}$$
$$\frac{\partial^2 I_0(kr)}{\partial r^2} = k^2 I_0(kr) + \frac{kI_1(kr)}{r}$$

A.2 Derivatives of H_θ and φ

The components of the boundary conditions given in equations 3.32 and 3.33 are

$$
\begin{aligned}
\frac{\partial \varphi}{\partial r} &= -k_1 \varphi_0 I_1(k_1 r)\cos(\xi z - \omega t) \\
\frac{\partial^2 \varphi}{\partial r \partial z} &= k_1 \xi \varphi_0 I_1(k_1 r)\sin(\xi z - \omega t) \\
\frac{\partial^2 \varphi}{\partial r^2} &= \varphi_0 \Big(k_1^2 I_0(k_1 r) + k_1 \frac{I_1(k_1 r)}{r} \Big)\cos(\xi z - \omega t) \\
\frac{\partial^2 \varphi}{\partial t^2} &= -\omega^2 \varphi_0 I_0(k_1 r)\cos(\xi z - \omega t) \\
\frac{\partial H_\theta}{\partial r} &= H_0 \Big(- k_2 I_0(k_2 r) - \frac{I_1(k_2 r)}{r} \Big)\sin(\xi z - \omega t) \\
\frac{\partial^2 H_\theta}{\partial r \partial z} &= \xi H_0 \Big(- k_2 I_0(k_2 r) - \frac{I_1(k_2 r)}{r} \Big)\cos(\xi z - \omega t) \\
\frac{\partial^2 H_\theta}{\partial z^2} &= -\xi^2 H_0 I_1(k_2 r)\sin(\xi z - \omega t) \\
\frac{\partial^2 H_\theta}{\partial t^2} &= -\omega^2 H_0 I_1(k_2 r)\sin(\xi z - \omega t)
\end{aligned}
$$

A.3 Detailed derivation of equation 3.35

Inserting the above relations into the boundary condition for σ_{rr} gives

$$
\begin{aligned}
\sigma_{rr} &= -\lambda \frac{\omega^2}{\alpha^2} \varphi_0 I_0(k_1 r) \\
&\quad + 2\mu \Big(\varphi_0 \Big[k_1^2 I_0(k_1 r) + k_1 \frac{I_1(k_1 r)}{r} \Big] \\
&\quad - \xi H_0 \Big(- k_2 I_0(k_2 r) + \frac{I_1(k_2 r)}{r} \Big) \Big) \\
0 &= -\lambda \frac{\omega^2}{\alpha^2 \xi^2 \mu} \varphi_0 I_0(k_1 r) \\
&\quad + 2 \Big[\varphi_0 + \frac{k_1^2}{\xi^2} \Big\{ I_0(k_1 r) + \frac{I_1(k_1 r)}{k_1 r} \Big\} + \frac{k_2}{\xi} H_0 \Big\{ I_0(k_2 r) + \frac{I_1(k_2 r)}{k_2 r} \Big\} \Big] \\
0 &= -b \vartheta_1^2 \varphi_0 I_0(k_1 r) + 2\varphi_0 (1 - \vartheta_2^2) \Big[I_0(k_1 r) + \frac{I_1(k_1 r)}{k_1 r} \Big] \\
&\quad + 2 H_0 (1 - \vartheta_1^2)^{1/2} \Big[I_0(k_2 r) + \frac{I_1(k_2 r)}{k_2 r} \Big]
\end{aligned}
\tag{A.1}
$$

Appendix B

Matlab Code

B.1 Roots of Bessel Functions

```
%Code used to find the zeros of the dispersion relation for Shear
%Horizontal waves.

%stainless steel properties
G=86e9; % shear modulus (in g/(m*s^2)
p=8000; % density (in kg/m^3)
sigma=0.29; % poisson's ratio
E=195e9; % modulus of elasticity (young's modulus) (in g/(m*s^2)
lambda = G*(E-2*G)/(3*G-E); % Lamè 1st parameter
a=4e-3; % radius of rod

beta=sqrt(G/p); % Shear wave speed
ka=-20:0.001:20;

nullpunkt=besselj(0,ka).*ka-2*besselj(1,ka);

%plot bessel
figure(1)
plot(ka, (besselj(0,ka).*ka-2*besselj(1,ka)))
grid on
axis tight
xlabel('ka')
ylabel('J_0(ka)*ka - J_1(ka)')
title('Bessel function')

%find roots the equation
j1=@(ka)(besselj(0,ka).*ka-2*besselj(1,ka));
zer_arr1=[0 5 8 12 15 18];
z1=zeros(1,length(zer_arr1));

for i=1:length(zer_arr1)
    z1(i)=fzero(j1,zer_arr1(i));
end
```

```
%create a phase dispersion relation plot
z1t=z1';
omega=3.5e6:10e3:10e6;
f=omega/(2*pi);
vp=zeros(length(omega),length(z1));
cutoff=zeros(length(z1));

for i=1:length(z1t)
    for j=1:length(omega)
        vp(j,i)=2*pi*f(j)*a/sqrt((2*pi*f(j)*a/beta).^2-(z1t(i)).^2);
    end
end

for k=1:length(z1)
    cutoff(k)=z1(k)*beta/(2*pi*a);
end

figure(4)
plot(f,vp/beta)
ylim([0 6])
xlim([min(f) max(f)])
hold on
plot(f, beta/beta, '-.k', 'LineWidth', 1)
hold off
xlabel('Frequency [Hz]')
ylabel('Normalized phase velocity v_p/\beta')
title('Phase velocities')
```

B.2 Rayleigh Surface Wave Dispersion Relation

```
% This file was created April 18th by Dragan Mitrevski after chatting with
% Evelyn Livermore on Facebook a late Thursday night and wanting to
% numerically solve the Rayleigh wave equation using MATLAB's fsolve
% instead of Maple's NewtonMethod.

% Modified by Evelyn Livermore for use in this master's thesis.

clc; close all;
nu = 0.0;
vu=0:0.1:0.5; % poisson's ratio
%s = 0.2957746479;
s=sqrt((0.5-0.29)/(1-0.29));
K0 = @(z)besseli(nu,z);
K1 = @(z)besseli(1,z);
f1 = @(x,y)(2*x.*y.^2/pi);
f2 = @(x,y)(4*sqrt(1-y.^2).*K0(pi*sqrt(1-y.^2)./x)./ ...
    K1(pi*sqrt(1-y.^2)./x));
f3 = @(x,y)(-(2-y.^2).^2.*K0(pi*sqrt(1-s*y.^2)./x)./ ...
    (K1(pi*sqrt(1-s*y.^2)./x).*sqrt(1-s*y.^2)));
f = @(x,y)(f1(x,y)+f2(x,y)+f3(x,y));

xVal = (0.01:0.1:0.9)'; % x-values
y0 = linspace(0.84,0.99999,length(xVal))'; % init y0
yVal = zeros(length(xVal),1); % allocate memory
opts = optimset('tolfun',1e-8,'display','off'); % optim opts
```

```
eF = cell(size(xVal)); % exit flags
op = cell(size(xVal)); % output struct (#it, etc)
fV = zeros(size(xVal)); % function value

for k = 1:length(xVal);
    x = xVal(k);
    [yVal(k) fV(k) eF{k} op{k}] = fsolve(@(y)f(x,y),y0(k),opts);
end

x = min(xVal):0.001:max(xVal); % x-values for interpolation
y = interp1(xVal,abs(yVal),x); % interpolation

figure
plot(xVal,abs(yVal),'ok',x,y,[min(x) max(x)],[1 1],'-k','linesmooth','on')
grid on;
ylabel('$v_p/v_s$','interpreter','latex');
xlabel('$\frac{\lambda}{2a}$','interpreter','latex');
```

B.3 Crosscorrelation

```
% Generate input signal and white noise. Find the crosscorrelated output
% signal in order to identify input signal.

fc=1e3; % Frequency of the gaussian pulse
fs=1000; % Sampling frequency
wn = 150*rand(1,fs+1); % Generate white noise
t=0:1/fs:1; % Generate time sequence
tc=0.5; % Center of Gaussian pulse, mean value of distribution
c2=0.001; % Variance
a=1/sqrt(c2*2*pi); % Amplitude
p=a.*exp(-(t-tc).^2/(2*c2)); % Generate Gaussian pulse
y=p+wn; % Output signal as input signal added to noise


figure(1)
plot(t,p) % Plot signal p(t)
xlabel('Time [s]')
ylabel('Amplitude')
matlab2tikz('gaussian_pulse.tikz');

figure(2)
plot(t,wn) % Plot white noise
xlabel('Time [s]')
ylabel('Amplitude')
matlab2tikz('white_noise.tikz');

% Find crosscorrelation
rpy=crosscorring(p,y);

figure(3)
plot(t,rpy) % Plot crosscorrelated signal
xlabel('Time [s]')
ylabel('Amplitude')
matlab2tikz('crosscorrelated_signal.tikz');
```

```
figure(4)
plot(t,y)
xlabel('Time [s]')
ylabel('Amplitude')
matlab2tikz('output_signal.tikz');


% This function estimates the crosscorrelation between the two functions x
% and y.

function [rxy]=crosscorring(x,y)


N1=length(x);
%N2=length(y);
rxy=zeros(1,N1);

for i=1:N1+1
    for j=1:N1-i+1
        rxy(i)=rxy(i)+x(i)*y(j+i-1);
    end;
end;
```

Appendix C

Ohlins Damper

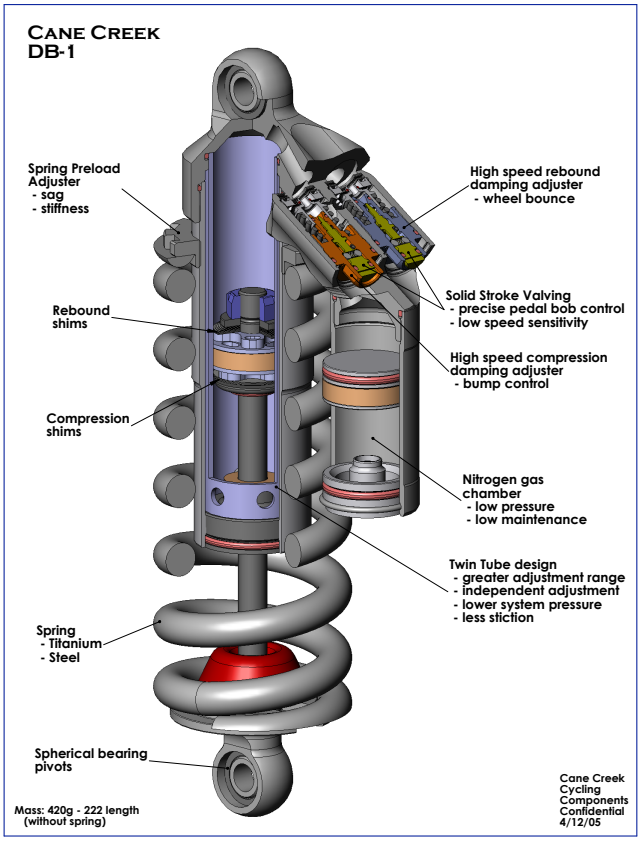

Figure C.1: Interior figure of damper

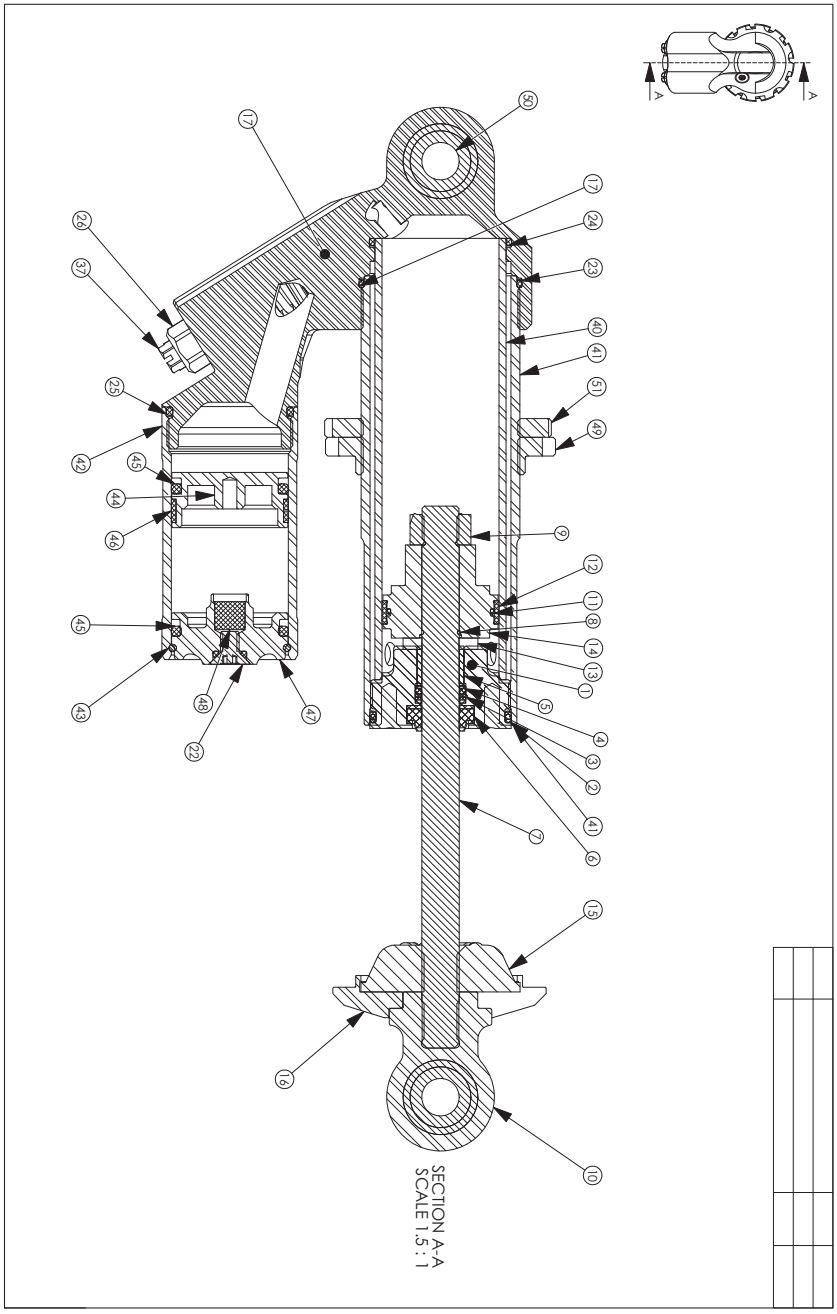

Figure C.2: Part description

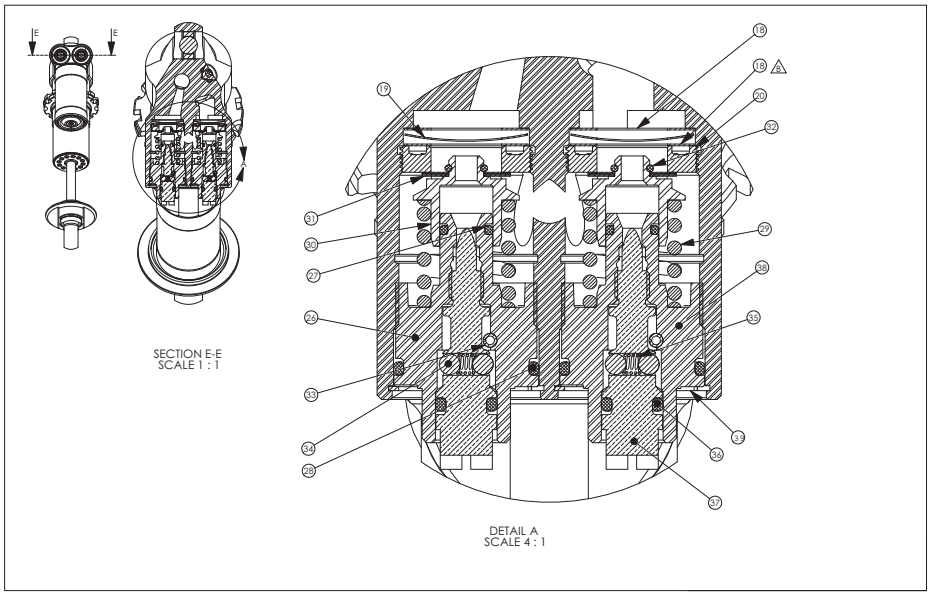

Figure C.3: Part description 2

Item No.	Description	Qty.
1	Seal Head	2
2	O-ring 26.7x1.78-a	2
3	Back Up Ring	2
4	Quad Ring	2
5	Bearing - Shaft	2
6	Rod Wiper	2
7	Shaft 115.8mm	1
8	CirClip 8x0.8-a	1
9	Lock Nut - M8	1
10	End Eye	1
11	O-ring 20.0x1.00-a	1
12	Piston Ring	1
13	Top Out Bumper	1
14	Piston	1
15	Bump Rubber	1
16	Spring Clip version 2.0	1
17	Cylinder Head	1
18	Shim - 00186-14	4
19	Wave Washer	2
20	Valve Seat	2
21	O-ring 4.5x1.50-b	2
22	Screw - flat head torx	2
23	O-ring 32.5x1.50-a	1
24	O-ring 28.0x1.50-a	1
25	O-ring 23.52x1.78-a	1
26	End Piece	1
27	O-ring 4.0x1.00-a	2
28	O-ring 13.5x1.50-a	2
29	Spring - valve 10N/mm	2
30	Poppet Valve	2
31	Shim - 4mm ID, T.15-10	6
32	O-ring 3.18x0.79-a	2
33	Spring Pin	2
34	Ball - Detent	4
35	Spring - Detent	2
36	O-ring 4.5x1.50-a	2
37	Adjustment Needle 2.2mm	2
38	End Piece	1
39	CirClip flat	2
40	Cylinder Tube - Inner	1
41	Cylinder Tube - Outer	1
42	Reservoir Tube	1
43	CirClip 25x1.60	1
44	Dividing Piston	1
45	CirClip 4.0x1.00	2
46	Piston Ring	1
47	Reservoir End	1
48	Seal - gas fill	1
49	Adjustment Nut - spring preload	1
50	Bearing - Spherical	2
51	Lock Nut - spring preload	1

Figure C.4: List of parts

Appendix D

Placement of new damper sensor

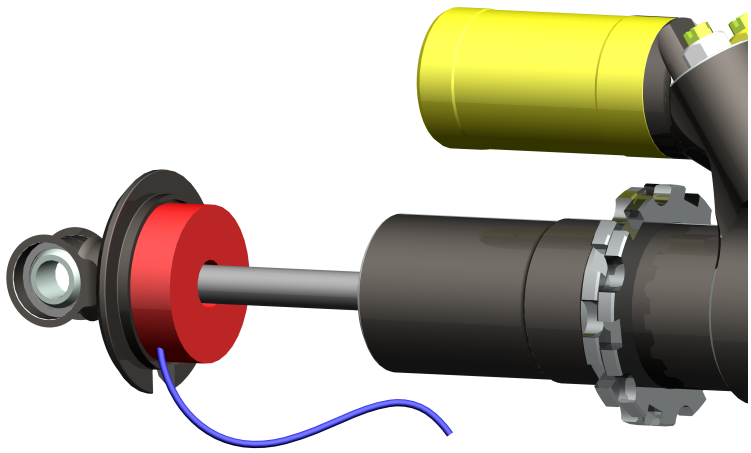

Figure D.1: pos2. Red=EMAT, blue=cable. Sensor size: outer diameter=32.6 mm, inner diameter=10 mm (1 mm liftoff), thickness=10 mm.

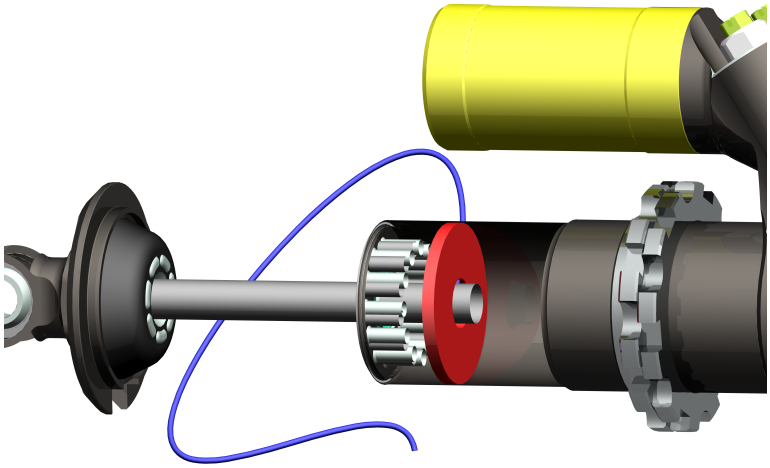

Figure D.2: pos3. Red=EMAT, blue=cable. Sensor size: outer diameter=32 mm, inner diameter=10 mm (1 mm liftoff), thickness=3 mm.

Appendix E

FEM models and results

E.1 Eddy current and magnetic field

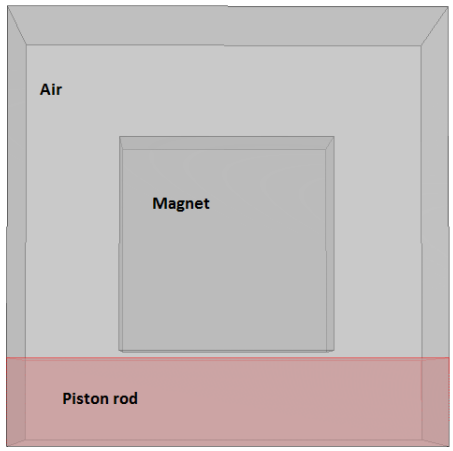

Figure E.1: Model used to simulate static magnetic field.

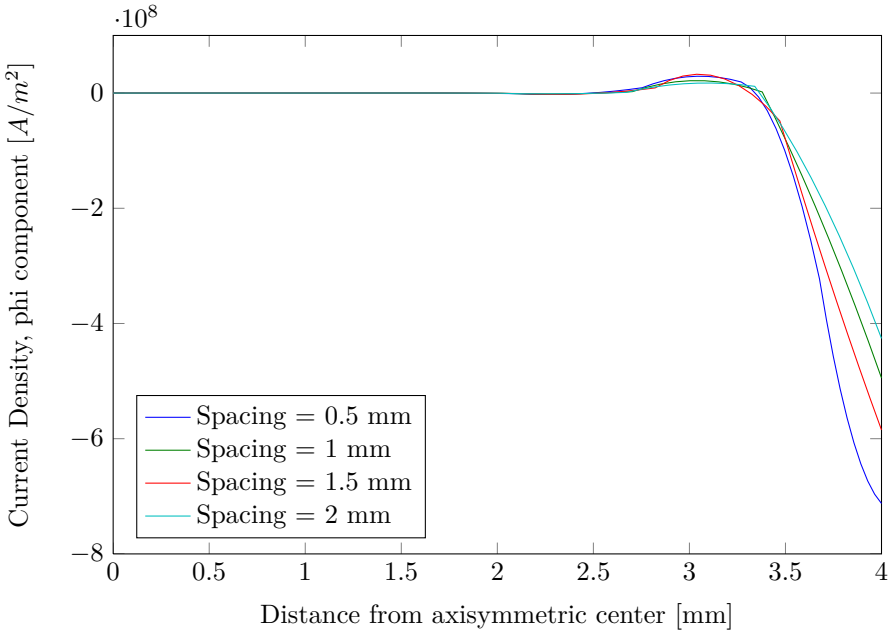

Figure E.2: Eddy current density for different values of spacing at 2.5 MHz.

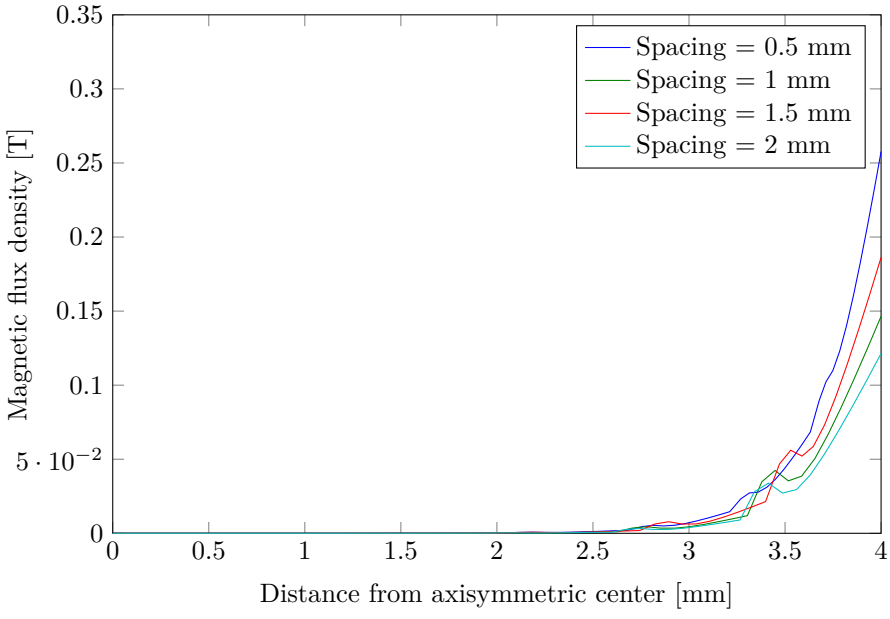

Figure E.3: Magnetic flux density for different values of spacing at 2.5 MHz.

E.2 Full simulation

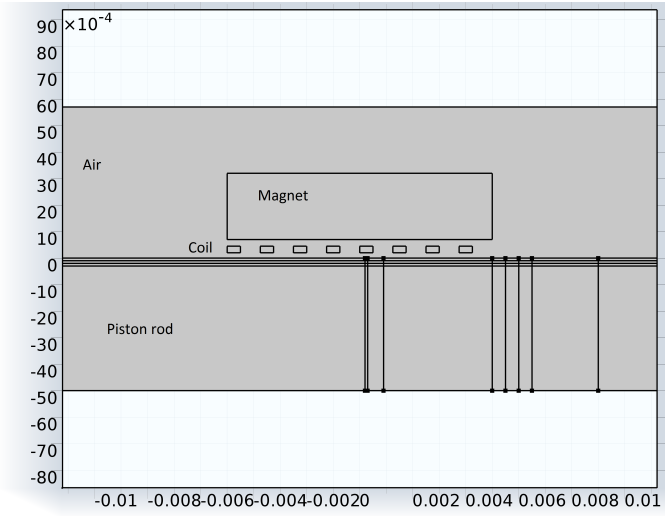

Figure E.4: Second geometry used for transient simulations. The vertical lines along the piston rod are help-lines for results, as well as the extra horizontal lines. The width of the coils is $500\mu m$, and height is $250\mu m$. The spacing between magnet and coil is $250\mu m$, and the liftoff to the piston rod is $200\mu m$. The spacing between the coils is $1mm$.

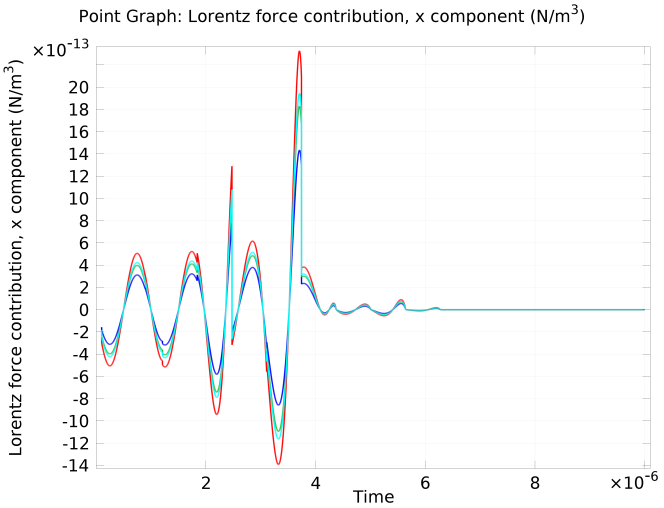

Figure E.5: Lorentz force contributor, vertical component. The plot is given for vertical points from piston rod top, amplitude in $[N/m^3]$.

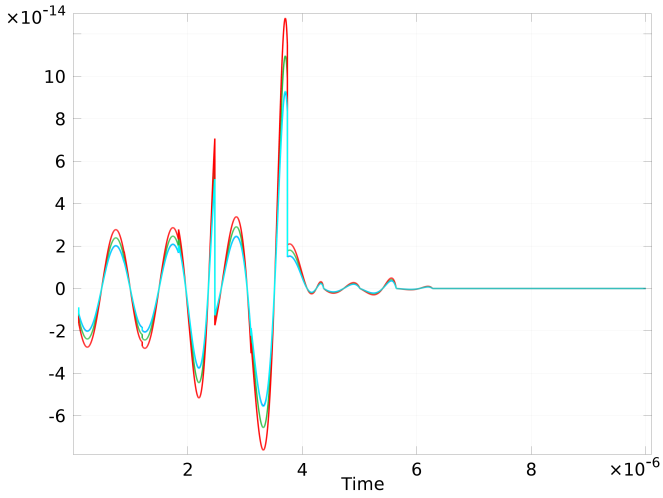

Figure E.6: Lorentz force contributor, horizontal component. The plot is given for vertical points from piston rod top, amplitude in $[N/m^3]$.

References

[1] Ahmad, R., Banerjee, S., and Kundu, T. Pipe wall damage detection in buried pipes using guided waves. *Journal of Pressure Vessel Technology 131*, 1 (2009), 011501.

[2] Association, M. M. P. Standard specifications for permanent magnet materials. `http://www.intl-magnetics.org/pdfs/0100-00.pdf`, 2012.

[3] Biot, M. Propagation of elastic waves in a cylindrical bore containing a fluid. *Journal of Applied Physics 23*, 9 (1952), 997–1005. cited By (since 1996) 85.

[4] Callister, W. *Materials science and engineering : an introduction.* John Wiley & Sons, Hoboken, NJ, 2010.

[5] Center, N. T. R. Emats. `http://www.ndt-ed.org/EducationResources/CommunityCollege/Ultrasonics/EquipmentTrans/emats.htm`, 2011.

[6] control, P. Racing sensors. Product Brochure, 2008.

[7] Dhayalan, R., Murthy, V. S. N., Krishnamurthy, C., and Balasubramaniam, K. Improving the signal amplitude of meandering coil emats by using ribbon soft magnetic flux concentrators (mfc). *Ultrasonics 51*, 6 (2011), 675 – 682.

[8] Dodd, C. V., and Deeds, W. E. Analytical solutions to eddy current probe coil problems. *Journal of Applied Physics 39*, 6 (May 1968), 2829 –2838.

[9] fang Zheng, M., Lu, C., zhu Chen, G., and Men, P. Modeling three-dimensional ultrasonic guided wave propagation and scattering in circular cylindrical structures using finite element approach. *Physics Procedia 22*, 0 (2011), 112 – 118. 2011 International Conference on Physics Science and Technology (ICPST 2011).

[10] Ferrari, R. Emat modeling in comsol. E-mail to Evelyn Livermore, 2012.

[11] Fukuhara, M., Kuwano, Y., Saito, K., Hirasawa, T., and Komura, I. Performance of non-destructive evaluation by diffracted sh ultrasonic waves in predicting degree of fatigue in cyclic bending of ferritic steel. *NDT International 31*, 3 (1998), 211 – 216.

[12] Giaraffa, M. Tech tip: Springs & dampers, part one. `http://www.optimumg.com/docs/Springs\%26Dampers_Tech_Tip_1.pdf`, 2012.

[13] Graff, K. *Wave motion in elastic solids.* Dover Publications, New York, 1991.

[14] Haznadar, Z. *Electromagnetic Fields, Waves, and Numerical Methods.* IOS Press, Amsterdam, 2000.

[15] Hirao, M. *EMATS for science and industry : noncontacting ultrasonic measurements.* Kluwer Academic Publishers, Boston, 2003.

[16] Hirao, M., Ogi, H., and Fukuoka, H. Advanced ultrasonic method for measuring rail axial stresses with electromagnetic acoustic transducer. *Research in Nondestructive Evaluation 5* (1994), 211–223. 10.1007/BF01606409.

[17] Jian, X., and Dixon, S. Enhancement of emat and eddy current using a ferrite back-plate. *Sensors and Actuators A: Physical 136*, 1 (2007), 132 – 136. <ce:title>25th Anniversary of Sensors and Actuators A: Physical</ce:title>.

[18] Johnson, W., Auld, B. A., and Alers, G. A. Spectroscopy of resonant torsional modes in cylindrical rods using electromagnetic-acoustic transduction. *J. Acoust. Soc. Am. 95*, 3 (1994).

[19] Johnson, W., Auld, B. A., and Alers, G. A. Trapped torsional modes in solid cylinders. *J. Acoust. Soc. Am. 100*, 1 (1996).

[20] Kawashima, K., Murota, S., Nakamori, Y., Soga, H., and Suzuki, H. Electromagnetic generation of ultrasonic waves in the absence of external magnetic field and its applications to steel production lines. *Ninth World Conference on Non-Destructive Testing; Melbourne; Australia; 18-23 Nov.1979* (Nov 18 1979), 8.

[21] Livermore, E. Microphotonic components in comsol. Project work, 2011.

[22] Lowrie, W. *Fundamentals of geophysics.* Cambridge University Press, Cambridge New York, NY, USA, 1997.

[23] NTNU, R. Homepage of revolve ntnu. `http://www.revolve.no`, 2012.

[24] Proakis, J. *Digital signal processing.* Pearson Prentice Hall, Upper Saddle River, N.J, 2007.

[25] Ribichini, R. Modelling of electromagnetic acoustic transducers. Master's thesis, Imperial College London, United Kingdom, 2011.

[26] Roozenburg, N. F. M., and Eekels, J. *Product Design: Fundamentals and Methods.* Wiley, Chichester New York, 1995.

[27] Yibo, L., Liying, S., Zhidong, S., and Yuankai, Z. Study on energy attenuation of ultrasonic guided waves going through girth welds. *Ultrasonics 44, Supplement*, 0 (2006), e1111 – e1116. <ce:title>Proceedings of Ultrasonics International (UI'05) and World Congress on Ultrasonics (WCU)</ce:title>.